Indoor Navigation Using Millimeter-wave Technology

Huyue Wang

A thesis submitted in fulfilment of the requirements for the degree of Master of Engineering in Computer System Engineering, the University of Auckland, 2022.

Abstract

In this thesis, a Simultaneously Localization and Mapping (SLAM) algorithm is designed for the purpose of indoor localization and navigation map generation using the millimeter-wave (mmWave) radio detection and ranging (radar) technology. The motivating application is ultimately to support firefighters or search and rescue team to explore and unknown environment that has low visibility due to hazardous smoke. The proposed system is designed to be self-contained and uses only a single mmWave radar to sense the environment. In comparison with other fused techniques, like working with Inertial Measurement Unit (IMU), this system is using Iterative Closest Points (ICP) algorithm to work out the displacement information, i.e. rotation and translation. The system does not require any prior knowledge of the environment, nor pre-installed infrastructure. The system is evaluated in a commercial building with a square shaped corridor. Three experiments with different walking paths are conducted to evaluated and demonstrate that the system is able to achieve reliable results with submeter accuracy. However, the system performance does decrease with travelling distance, which requires further investigation in the future.

Acknowledgement

I would like to express my great gratitude to my supervisor Dr. Kevin I-Kai Wang for his valuable guidance and support throughout the research.

Thanks to the examiners for their feedback and advice, and all the staff and members of the university who kindly offered their assistance.

And always thanks my parent for their endless care and love.

Table of Content

1. Introduction

The geographical position information of users is commonly obtained and used to provide the Location Based Services (LBS), which include directory service, gateway service, and location utility service, etc. [1]. The topic around localization system became popular and have been frequently discussed since the Global Positioning System (GPS) is firstly introduced in the 1970s by the United States government and became accessible worldwide for civilian applications in the 1980s [2], [3]. The GPS is based on using satellites to achieve its wide coverage and the target location is determined through triangulating the received space and time signals from at least three satellites.

Due to its wide coverage and availability, GPS has dominated the majority of outdoor positioning and navigation applications. However, it is facing a challenge as the usage of it requires the line of sight (LoS) to multiple amounts of satellites to achieve the full capability [4], [5]. Therefore, the Global Message Services (GSM)-based outdoor positioning technology which was deployed on a cellular network and accessed by cellphone is introduced in 1992 as a complement when GPS is not available [6] [7]. This positioning method measures the signal strength from the base station to a user's cellphone, and locate the geographical point through triangulation or multilateration in a single cell. The hybrid of GPS and GSM eventually become a popular option, and many research efforts and techniques have been proposed for outdoor localization as access to smart devices is easier than ever [8]–[10]. However, these systems mainly focuses only on outdoor applications due to the limited and interfered indoor reception of satellite and cellular network signals.

In modern days, the position information is frequently acquired as it offers valuable insights that can assist our daily activities. The indoor positioning is highly beneficial to Internet of Things (IoT) and home automation applications by offering real-time location information to the gateway devices. For instance, the research [11], [12] shows the investigation toward the aspect of mobile robot localization and the collection and analysis of path pattern in an indoor environment, and the research[13], [14] is illustrating how the positioning information could use to improve the assisting of the elderly and telecare for home automation.

Although the GPS and GSM can be used to provide localization information for both outdoor and indoor purposes, they are still limited due to the loss of accuracy in indoor conditions. The research shows people are likely to spend up to 80% of their daily time in indoor environment which raising interest in the technologies like Indoor Positioning System (IPS) and personal radar, which are used to

provide position and landmark information for both objects and surroundings within a room [15], [16].

The indoor environments are enclosed by walls and ceiling which block the satellite signal. This leads to significant performance reduction for GPS-based outdoor localization technologies such as like Global Navigation Satellite System (GNSS). In addition, the coarse spatial resolution offered by GPS-based technologies also does not satisfy the needs for indoor applications, where finer motions are required to be detected to fully analysis the trajectory or behavior [17]. Similarly, there are some existing research toward the GSM-based indoor positioning, but they also suffer from the attenuation caused by buildings and have limited performance[18]–[23].

Indoor environment is often more complex than the outdoor environment. For example, various obstacles (walls, furniture, and occupants) result in a more reflective environment which leads to issues such as multipath fading of wireless signal [19]. Recently, there are many researches on different indoor positioning systems using WIFI [24]–[27], Bluetooth [28], [29], Infrared (IR) [30], [31], and ultrasound [32], [33]. Other notable techniques are the IMU and a series of radar sensors, which can provide the trajectory information or the scanning of the environment to the poisoning system respectively [34]–[37] . However, those techniques are always working as a part of a larger system, which is used as a fused technique, due to it is hard to construct a concrete positioning outcome solely by their measurement. In practice, different technologies have different shortcomings in various indoor positioning and navigation applications, and till now there is still no universal solution.

Typically, a positioning problem can be categorized as either localization or mapping, for instance, localizing the position for navigation purpose or mapping the environment to determine the location of fixed infrastructure or objects. The localization refers to the process of determining one's position, and the mapping means depicting the feature of the surrounding environment with the knowledge of walking path [38], [39]. However, prior knowledge of any given environment or pre-installation of any measurement/sensing infrastructure is very rare and/or costly. Therefore, it is important for an IPS to be able to operate in an unknown environment without relying on any prior installation of sensing devices.

In this thesis, a SLAM algorithm will be proposed as a solution for the indoor exploration under unknown condition, as it is able to estimate the position while exploring the environment and constructing a map at the same time. The SLAM problem is firstly introduced in 1991 and an Extended Kalman Filter-based (EKF) SLAM solution has been proposed at the same time [38], [40]. Another significant filter-based SLAM algorithm is the Particle Filter-based (PF) solution, which helped with covering the non-linearity issue of the SLAM problem [41], [42], and in 2002, a fusion algorithm of EKF and PF was proposed [43]. Rather than filter-based solutions, there are also some graph-based algorithms that try to solve the SLAM problem in a view of the graphical model such as [38], [43],

which will be discussed in Chapter 4.

Currently, one of the most popular technologies for collecting data in indoor scenarios is optical-based solution, such as stereo-camera, or laser-based radar (i.e. lidar). However, both options have significant drawbacks in indoor conditions, for example, the stereo-camera is highly vulnerable to the lighting condition especially when a significant illumination transition present in the environment [44]. Similarly, the lidar sensor also require a good visibility of the environments, as it could be affected by the dust and unclear field of view (FoV).

Therefore, in this thesis, a state-of-art mmWave radar has been chosen as the solution for an indoor positioning system due to its unique features that can overcome the aforementioned limitations of poor visibility.

In addition, considering the indoor SALM, it is important to reduce the size of the data collecting device and avoid the data integration, as the portability and the computational cost should be evaluated. Instead of using traditional localization devices, like the GPS and IMU, the iterative closest point (ICP) algorithm is used to work out the movement of the target. The ICP is an iterative algorithm that has been widely used to minimize the geometric difference between two sets of cloud points data in three dimensions [45]. In this project, the ICP is used as the replacement of IMU to provide the translation and rotational matrix that help with building the map.

The goal of this research is to investigate and propose a SLAM algorithm that enables a human to explore and navigate an unknown indoor environment using only a single mmWave radar. A wearable mmWave radar collects and provides point cloud data, which is subsequently processed by the SLAM algorithm to produce a map. The proposed system offers an infrastructure-free and seamless service that is able to trace human position and to map the surrounding environment simultaneously, which is helpful for navigating both unknown and familiar physical environment.

In the rest of the thesis, the Chapter 2 provides an overview of some fundamental positioning techniques with their pros and cons. This Chapter introduces the fundamental theory of positioning, including how the distance between the obstacle and the target could be evaluate and how the coordinate (i.e. (x,y) for 2D condition) of the obstacle could be sensed.

In the Chapter 3,, a variety of indoor positioning technologies will be introduced and compared to demonstrate why mmWave is chosen and what are the advantages of using it.

The Chapter 4, will start with a basic introduction of the SLAM algorithm, the details on the proposed algorithm will also be described in this Chapter.

The Chapter 5, is reported with particular specific on the technology and ideal related to the device that used in this research, IWR 1443 mmWave Sensor [46], The information of IWR 1443 includes the analysis of the parameter setting, device features, working flow, data structure, and the mathematical theory of the radar. In this chapter, an overview of the radar device will be presented with the basic ideal of radar theory

In the Chapter 6, the technical detail of the ICP algorithm will be explained, this section will be focusing on the mathematical theory behind the algorithm and a demonstration of the ICP algorithm will be shown.

The Chapter 7 is the system implementation, it is mostly about the procedure code, and the system architecture. This section will explain how the whole system working, and the parameter selection, a flowchart will also be used to demonstrate the system working flow.

The Chapter 8 will mainly discuss the result of different experimental trials. This chapter involves the compare and contrast of the outcome for each experimental set under different conditions based on certain criteria that are used to evaluate the system performance.

Moreover, the visualized final experimental result will be shown in this chapter, and based on the result, the comparative trials, for example, compare the system outcome with the ground-truth will be reported.

In the last of the thesis, the result of the comparative experimental trials will be discussed in this section to generate an overall conclusion to verify and justify the system to conduct if the system is a reasonable solution for the task of indoor localization and mapping. In addition, any potential improvement strategy or further investigation direction will also be presented in this chapter.

2. Fundamental Localization Techniques

To determine the position of a target, the ability to sense the environmental information is essential. Therefore, at least one kind of rangefinder should be used. As mentioned in the previous Chapter, radar system will be the primary focus in this thesis. A working radar system should contain at least two parts, which are the transmitter and receiver, and they are used to emit certain signal and receive the returning reflected signal from an object respectively [47].

In this case, some attributes of the signal that is sent and received by the antennas are used to compute the location information. In this thesis, some fundamental positioning (or localization) techniques will be discussed, and they can be categorized into two types, the Time and Space Attributes of Received Signal (TSARS)-based method, and the Received Signal Strength (RSS)-based method [16]. In the following subsections, these techniques will be introduced and discussed.

2.1 The Angle of Arrival

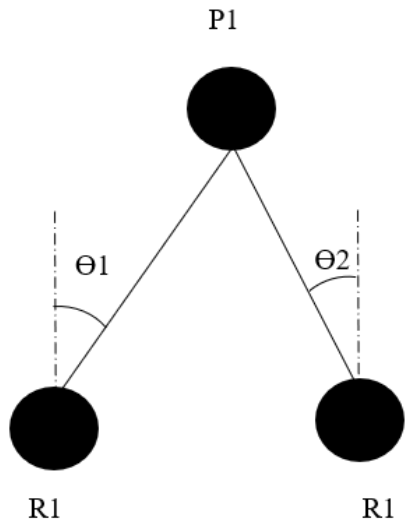

Figure 2.1: AoA Measurement

The Angle of Arrival (AoA) is a TSARS based approach that determines the arrived signal direction by performing the measurement and calculation to estimate the angle of signal impinge the antenna array [16]. Generally, the signal direction will be calculated by the phase or time difference of the arrived signal sensed by individual antenna within an array. Referring to Figure 2.1, based on the estimated arrival angles, the intersection point is considered as the estimated target location [16]. In other words, an AoA system can determine target's location through the signal received by base stations or antenna arrays at known geographical locations.

Figure 2.1 illustrates a simple AoA measurement, in a two-dimensional situation, at least two anchor nodes will be required to obtain the signal direction. The reference points R_1 and R_2 can be used to determine the position of target P_1 by extending a line in the direction with the measured arrival signal angle, the intersection point of the lines will be treated as target location. To improve the accuracy, additional reference points could be added for triangulation.

Although the AoA measurement is a time-synchronization-free option and can achieve a submeter accuracy, from 0.5 to 1m, it requires more complex hardware equipment and calibration [48]. The accuracy may also be deteriorated when the target distance increases, due to measurement error is amplified during the process of calculating the estimated location. In other words, a slight error in measurement will cause a large deviation in the location [49]. In addition, the LoS is required by AoA-based method, it is usually hard to fulfill in indoor conditions due to the severe multipath effect, and this property significantly limits the interest for AoA in indoor applications.

Based on the AoA localization technique, several algorithms are developed in existing literature. For example, the Multiple Signal Classification (MUSIC) algorithm which returns the decomposed components of the autocorrelation matrix is widely used to obtain the angle of different arrived signals. The MUSIC algorithm is popular for its good performance at low signal to noise ratio (SNR) [25][50]. Unfortunately it is unable to determine the existence of different LoS. Therefore, to identify the LoS of an arrived ray, another algorithm named the Joint Angle and Delay Estimation (JADE) is proposed to handle the situation when a single antenna needs to process multiple signals [50][51]. The JADE algorithm can distinguish the arrival angles of rays with LoS from other multipath rays, but it is also most costly because more resources and hardware support is required.

2.2 The Time of Arrival

The Time of Arrival (ToA) is another TSARS-based approach that estimates the location of the target device by measuring the propagation time of the signal between target object and the anchor device that located on a known geographical location. Therefore, the synchronization between the transmitter and receiver is required to accurately calculate the travel time. The physical distance (i.e. the range between the sensors) can be determined by the product of propagation time and the speed of the signal as shown in Equation 2.1 [49].

$$d = c \times t \tag{2.1}$$

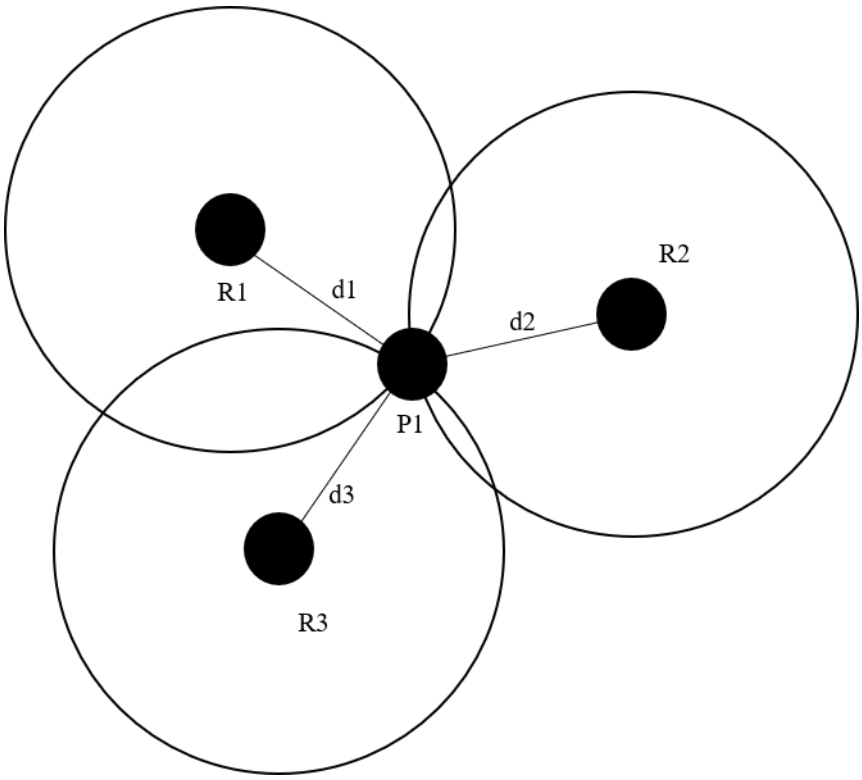

Figure 2.2: ToA Measurement

Although the mentioned process can potentially be performed with a minimum of two reference points, in practice, the basic geometry method, like trilateration, is used to eliminate ambiguity, which means at least three anchor devices are required [52]. In Figure 2.2, the location of the target object P1 is determined by the intersection of those circles which are centered at the reference point R1, R2, and R3, with the radius (d_1, d_2, and d_3) calculated from Equation. 2.1 using the prorogation time of the signal.

However, due to errors in range estimation, the intersection of the circles could always result in a region instead of a precise point. To improve the performance, Weighted Least Square (WLS) or Least Square (LS) is used to overcome the gap between the most probable position with the consideration of some error and the raw estimated location. Traditionally, this is not an issue with outdoor localization applications due to coarser spatial resolution for outdoor applications. However, the ToA-based methods that suffer from limited accuracy are less likely to satisfy the finer location precision required by indoor localization applications.

On the other hand, the accuracy of ToA also depends on the bandwidth and the sampling rate [16], [25], and hence the measurement also introduces error. For instance, in Figure 2.3, there is an interval between the signal arrived and the system taking the measurement, and when the sampling rate of the system is 10MHz, and an error of around 30 meters will be introduced.

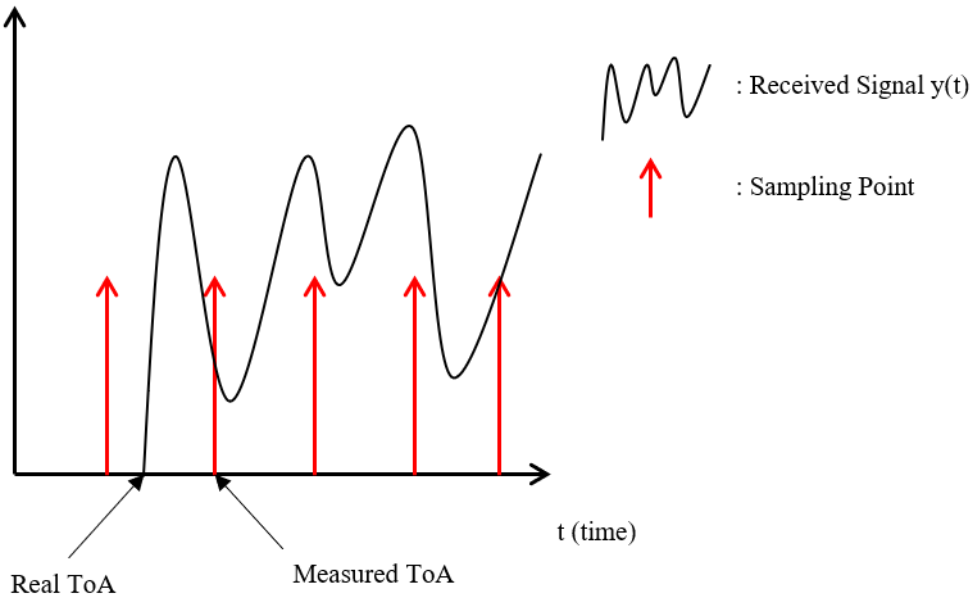

Figure 2.3: ToA performance vs transmitter bandwidth

2.3 The Time Difference of Arrival

The Time Difference of Arrival (TDoA) is also a TSARS-based approach that estimates the location using the time difference among each receiving anchor node. Different from ToA, TDoA-based

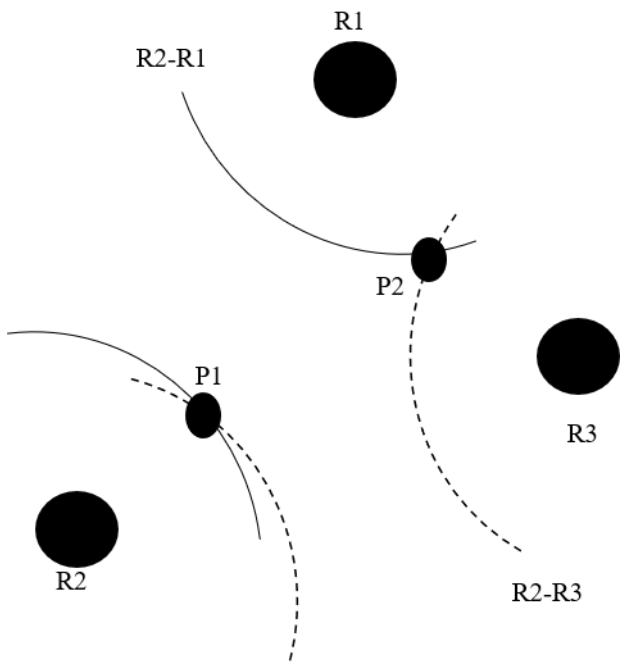

Figure 2.4: TDoA Measurement

approach does not require synchronization between the sender and receiver. For instance, in Figure 2.4, there are two pairs of hyperbolas that demonstrate the possible position of the object P between R1, R3, and R2. The solid one indicates the possible position of the object calculated by Equation 2.1 using the value of t, the difference of the signal received in time between R2 and R1, Similarly, the doted one is using the time difference of the signal received between R2 and R3. From the graph, the intersection of those two curved lines could be found can could be ladled as the position of the object. In this figure, two points are given as the solution, as the presenting of error and the intersection of hyperbolas can be more than one, which are the ambiguous point P1 and calculated position P2. To improve the performance, an extra measurement can be taken, in this case, the possible position with the time difference between R1 and R3 could also be calculated to get a more concrete point of the intersection.

Compare with ToA, instead of measuring the propagation time of signal, TDoA use of the time difference of a signal arriving at two reference points. The difference in arrival time between the two reference points can be expressed as:

$$t_1 - t_2 = \frac{R_1}{c} - \frac{R_2}{c} \tag{2.2}$$

where t_1 and t_2 are the signal arrival times at two difference reference points, R_1 and R_2 are the distance between the signal source and a reference point, and c is the speed of the signal.

In 2-dimensional case, the distance between two reference point can also expressed as:

$$R_{i,j} = \sqrt{(x_i - x)^2 + (y_i - y)^2} - \sqrt{(x_j - x)^2 + (y_j - y)^2} \tag{2.3}$$

where $R_{i,j}$ is the physical distance between reference point i and j, (x, y) representing the x and y position in 2-D coordination.

Equation 2.3 allows us to find a hyperbola that reveal the potential location of the target under a fix distance [16], [23], [52], [53].

2.4 RSSI & Fingerprint

In indoor conditions, some measurements such as the propagation time and the received angle could be seriously deteriorated by the multipath effect caused by the radio propagation between the transmitter and receiver. Alternatively, in some approaches, the strength of the signal is measured as a replacement of the arrival time or angle of the signal.

The Received Signal Strength Indicator (RSSI) is a relative measurement of received signal strength, which reflects the distance information from the transmitter to the receiver. For this kind of localization technique, a centralized or distributed synchronization system might be needed for the overall received signal strength (RSS) collection and calculation [16].

Typically, the RSSI can be modelled as:

$$RSSI = -10n \log 10\,(d) + A * RSSI = -10n \log 10\,(d) + A \tag{2.4}$$

where *d* refers to the distance between sender and receiver, and n is the path loss exponent that is selected from 2 to 4 for emulating free space condition and dense environment respectively. The A is the RSSI value at reference distance (usually 1 meter).

Referring to Equation 2.4, the distance, d, between the sender and receiver can be found. In practice, at least three reference points (and hence three ranges) are necessary so that techniques such as trilateration can be applied with RSS measurements. This is similar to Figure 2.2, where the nearest three anchor points are selected as ‘centre’ and the circles are drawn with a radius calculated based on the received signal strength [16], [54]. The intercept between those three circles will be found and gives the estimated location. The intersection between those three circles gives the estimated location. The RSSI-based localization technique is also known for its low cost and ease of deployment. However,

with RSSI and trilateration alone, it also suffers from low accuracy as the complex indoor environment can cause a severe multipath fading [16].

The RSSI alone approach could only offers a coarse estimate, one potential solution is proposed to improve the precision by combining the RSSI with fingerprinting/scene analysis technique [25]. Fingerprinting is a site-survey based approach which includes a priori 'environmental scanning' and real-time measurement. The fingerprinting strategy always contain two parts, which are online phase and offline phase. The offline calibration phase build-up a signal intensity map according to the pre-measured RSS. This process involves the collection of measured RSSI value from every potential location to construct a RSSI map. The online phase will then compare the real-time RSSI data with the offline map to determine a location estimate.

However, the accuracy of fingerprinting strategy is largely dependent on the size of grid where the RSSI can be measured and distinguished in practice, and the smaller the grid size the higher the accuracy [55]. Once the system is online, the real-time measurement will be performed to match the offline map and find the possible location through several algorithms, such as probabilistic, deterministic, and other methods [54]. For example, the Nearest Neighbour method can be considered as a deterministic method as it calculates the distance between the real-time device signal strength and the matched intensity vector in the database using the Euclidean metric. In addition, the K-Nearest Neighbour (KNN) method can offer better accuracy, as the K (typically K =4) best matches the intensity map database used to work out the average position [8]. For instance, the work in [54] shows that within the scale of 0.5-meter rectangular grid cell, 90% estimated results given by the KNN algorithm can achieve an accuracy which is within 1.5 meter from the ground truth. Although more anchor nodes can be used to increase the performance, the raw fingerprint system can operate with a single anchor condition, as the fingerprint is a unique set of signal properties that the anchor node will receive from a certain position due to complexity of indoor condition and multipath effect [25], [54]. Therefore, the receivers can capture the estimated location by searching the most similar fingerprint from the database rather than using the trilateration method. Based on this property, the number of required anchor devices for each grid can be reduced.

3. Localization Technology

Basically, the IPS can be categorized into two types, which are the active and passive systems. Both systems require some degrees of pre-installed infrastructure within the indoor environment [56]. However, an active system could require a device to be mounted on the user (or target object) and may need some degrees of corporation from the target object through the device. In contrast, passive systems only require minimal or no participation from the end devices. In the extreme case, the target object does not even need to carry a tracking device. The performance of different type of localization technology will be discussed and compared based on the following merits:

(a) Accuracy

Localization accuracy is the primary performance metric for evaluating different indoor positioning systems. This term refers to the proximity between the estimated and the actual location. Typically, the Euclidean distance between the estimated location and the actual target location will be used to evaluate the accuracy.

(b) Complexity

In general, the complexity consists of three elements, which are the deployment of physical devices, the processing of the raw sensing signals, and the computation of the localization algorithm. In this research, we mainly focus on the last two elements to measure and compare the differences between different localization technologies.

(c) Coverage

The coverage refers to the distance or area a localization system can support with promising accuracy. This performance metric will be adopted from existing literature or calculated by the radius of one single anchor node to compare different localization technologies.

(d) Scalability

The scalability refers to the cost for modifying the existing system deployment to a larger coverage.

(e) Adaptiveness

The environmental variations could significantly impact the system's performance. Therefore, the term adaptiveness indicates the ability to cope with the dynamic changes of the environment, such as the flow of occupants, temperature, and moving of furniture or other obstacles.

(f) Cost

For indoor localization systems, the cost could include not only the financial expenditure but also the time spending on the installation and maintenance of the physical deployment. Therefore, the cost factor of a localization system could also reflect the complexity of the distribution of the physical devices.

3.1Wi-Fi

Wi-Fi is a wireless local area network (WLAN) that is widely deployed in our modern society. Due to the wide adoption and availability, Wi-Fi-based IPS is also very popular. The Wi-Fi-based IPS is based on radio frequency technology, and uses radio signal operating at 2.4GHz or 5GHz bands with a typical coverage of around 100 meters. The IEEE 802.11 standard allows a Wi-Fi access point to be also used as an anchor point as it is able to measure the signal intensity without physical extension.

In addition, most Wi-Fi-based IPS is using fingerprint techniques as it is promising, low-cost (i.e., can be deployed without any extra hardware modification under existing Wi-Fi networks), and with high precision. Therefore, the fingerprint combined with the RSSI technique is the primary focus of Wi-Fi-based IPS. This because the measurement of the signal intensity also has a relatively low computational cost, and have a better performance under the low-consumption condition [16], [57].

The research in [24] shows that a deterministic RSSI and fingerprint indoor positioning method can achieve an accuracy around 0.1 to 0.5 meters. However, the RSSI-fingerprinting-based Wi-Fi positioning system has a relatively high algorithm complexity as it requires more computational support, and the usage of fingerprinting method makes this type of systems more vulnerable to external changes. The variation not only means the changing of the big obstacle like the furniture, wall, and any large objects, but also includes moving occupants. The dynamic of human movements could lead to an increase of error by 11% in general as the signal operated in the 2.4 GHz band can partially be absorbed by water, which accounts for 70% of the human body [57]. Moreover, the research also indicated that the change in temperature can also impact the signal intensity and showed that Wi-Fi signals are sensitive to temporal variation, which means the localization accuracy could reduce with a distant time proximity [58].

To achieve optimal utilization of Wi-Fi, smart devices like laptops and smartphones are commonly used as positioning devices [24], [25], [58]. However, the device heterogeneity among different vendors of devices could cause a different received signal strength measurement at the same reference

point, according to the findings in [24], the difference of RSS measurements between different brands of smartphones can be as large as 20 dBm.

For active Wi-Fi IPS, the largest problem is it may require some cooperation from the user's side. This means the overall performance could vary significantly without the participation of users and may increase security risks due to lack of the ability to anonymize localization targets.

Therefore, the interest for passive localization systems rises as it provides a potential indoor positioning solution with less involvement from the user and hence be able to minimize the computational requirement on user's devices. For example, some existing research proposed using an RSSI-fingerprinting-based passive Wi-Fi IPS through the passive signal diagnosis from the access points [15] [27]. The proposed system estimates the position of the target object through the RSSI of the Wi-Fi beacon, which is a periodical signal emitted from the mobile devices that used to find the nearby access points and contain the MAC address of the device. Such system can achieve an average accuracy of about 3.72 meters with a 10-15 second Wi-Fi beacon transmission interval. Moreover, with further improvement, an unsupervised online fingerprint collecting method is proposed, which significantly increases the scalability and adaptiveness of RSSI-fingerprint-based Wi-Fi indoor positioning as it offers the ability against environmental changes. However, the online method could also introduce an error around 2.93 meters when generating the radio map, which decreases the overall accuracy [27].

3.2 Infrared

The IR is a type of radiation with a wavelength longer than visible light, which can be considered as an optical technology. An IR-based IPS typically contains an IR light emitter that transmits the IR signal, and a receiver (or sensor) to receive the IR signal. Typically, a light-based indoor positioning system (LIP) consists of emitters (or sometimes referred to as LEDs) and receivers (or sometimes referred to as photodiode or photo sensors).

The active beacon is a popular approach for exploring the IR signal, which the signal receivers are fixed at a known location to sense the IR signals emitted from beacons that are placed on each target. For instance, an Active Badge system is a widely deployed IR-IPS where an electronic identification device, the badge, is used to emit a unique IR signal every 15 seconds. The sensors will be placed at predetermined locations to collect IR signals with a fixed period [52].

The performance of IR-IPS could be affected by many ambient properties, for instance, IR-based systems highly depend on the LoS condition between the emitter and the receiver because IR signal can

be easily blocked by non-transparent obstacles [49]. Moreover, the IR signal can also be influenced by reflectivity, scattering, and ambient light[49].

Compared with a Wi-Fi-based system, the LIP system is more suitable for electromagnetic-sensitive scenarios, such as the intensive care unit (ICU) or airport, as it does not produce any electromagnetic interference. The main advantages of using IR-IPS is its lightweight and the cost for the devices is relatively low [15]. However, the cost for the system could be high as the IR technique has limited coverage, and hence many LEDs or photo sensors need to be installed to ensure good coverage and performance.

Different to active IR systems, the IR-based passive positioning methods take advantage of the indoor scenarios as human bodies are natural IR sources. In general, passive IR (PIR) sensor is the most widely used device in IR-based passive indoor localization systems, multiple PIR sensors could be used to sense warm objects and compose a global field of view for detecting the direction of movement [32]. Therefore, the accuracy of passive IR indoor positioning is highly dependent on the density of sensors deployed and their overlapping for constructing the global map [32].

For instance, a PIR-based indoor positioning system combined with grid-based accessibility map is investigated.

3.3 Ultrasound

Ultrasound is a sound wave-based technology that uses sound with a frequency higher than the audible range. Typically, an ultrasonic-based positioning system operates at a frequency range between 40 - 75kHz and can reach a coverage of up to 10 meters [52]. The ultrasound based IPS are characterized by its low system cost and high accuracy, but it is more susceptible to environmental changes as the speed of sound could vary with humidity and temperature.

The Active Bat system is a popular ultrasonic IPS that utilizes a wearable small tag as the emitter to generate the ultrasound signal. An ultrasonic IPS typically measures ToA or ToDA introduced in the previous chapter to determine the distance between the emitter and receiver. Based on detected distances, at least three microphones (sound sensors) are required in order to use trilateration to compute the estimated target location.

The main advantage of an ultrasonic system is that it is not heavily constrained by the LoS condition measurement [20]. However, it is limited by its coverage and cannot propagate through thick walls.

The limited coverage is the main drawback of ultrasonic systems' scalability because a large amount of hardware infrastructure will be required for an ultrasonic system.

Different to active ultrasonic systems, Echolocation is an example of a passive positioning technology that measures the reflected acoustic signal from a surface or object and estimates object locations based on the characteristics of the echo signal [32]. This system utilized a single acoustic transmitter and four receivers around the speaker that were on the center of the board [47]. The reflected signal received by the microphone array (i.e. the four receivers) is then processed to work out the relative transmission time, compared with the timing of the signal being transmitted. At last, the processed signal profile will be compared with the reference, an empty room impulse response, to find out the estimated location of the target.

3.4 Bluetooth

Bluetooth is a wireless communication technology that operates in the 2.4GHz Industrial, Scientific and Medical (ISM) band. Bluetooth is typically used to establish a so-called personal area network that interconnects multiple personal devices. Due to the bloom of smart personal devices, a newer version of Bluetooth technology, Bluetooth Low Energy (BLE) has been released.

The BLE offers superior low power consumption with reasonable coverage at 70 to 100 meters in comparison with the older versions of Bluetooth. In practice, two RSSI-based BLE localization technologies, Eddystone and iBeacons (proposed by Google Inc. and Apple Inc. respectively), are widely deployed on smartphones [59], [60].

For example, an iBeacons system consists the one-way iBeacon transmitter, which emit a signal with 16 bytes Universally Unique Identifier (UUID), and a receiver will be used to pick up the compatible signal [59]. The position of the receiving end (e.g. a smart device on the target), could be determined by the corresponding app through the RSSI measurement of the arrival signal that sends by the iBeacon transmitter if it is located in a known place. In practice, the iBeacons system can achieve accuracy with 2.22 meters under 40ms reacting time [53].

3.5 Millimeter Wave

The mmWave refers to radio frequency signals that operate between 30GHz to 300GHz spectrum, it is a wide spectrum that is less occupied [32] . The mmWave spectrum can support a wide range of

applications. For instance, the fifth generation of cellular networks (5G) is utilizing 28GHz, 38GHz, and 70-80 GHz bands [64]. Moreover, the recently developed IEEE 802.11ad standard allows Wi-Fi to operate at the 60 GHz band [32].

For indoor positioning scenario, 60GHz is a commonly used spectrum, the high atmospheric absorption and high path loss nature of this spectrum makes it an ideal option for positioning due to those properties could largely reduce the self-interference. Technically, the double-bounce reflection is the maximum multipath signal that a mmWave channel can take because the higher-order bouncing signals suffer from severe attenuation at this frequency range, which means the LoS propagation path can be easily distinguished [32]. Moreover, the beamwidth ranges between 7 and 10 degrees and has less energy scattering with reflection, which takes advantage of angular-based positioning method, such as AoA introduced in Chapter 1.1 [32].

As mentioned, the mmWave spectrum can also be used in future Wi-Fi and cellular networks, so there is an overlap between those technologies, which offers great potential in the aspect of indoor positioning. For instance, the research suggests 1.32 meters of accuracy can be achieved through a RSSI-Fingerprint based indoor positioning method using a 60 GHz Wi-Fi system [62].

Regarding the passive method for mmWave technology, the interest of combining mmWave with SLAM has attracted a lot of attention due to the short wavelength of mmWave offers the ability to integrate a large number of antenna elements into a small device [32]. Therefore, there is a potential to bring mmWave-based radar technology into personal applications and indoor environment to provide the ability of target positioning along with mapping the environment [63]. Moreover, the short wavelength and the wide bandwidth can also increase the capability of handling multi-target scenarios which are very challenging using existing technologies.

	Accuracy (m)	**Coverage (radius, m)**	**Scalability**	**Adaptiveness**	**Cost**
Wi-Fi (Active) [16], [24]	1.2	~5.6	High	Medium	Low
Wi-Fi (Passive) [27]	1.2	~13	High	Low	Medium
IR (Active) [52]	2.3	~5	Low	Medium	High
IR (Passive) [31]	0.227	~1	Low	Low	High
Ultrasound (Active) [32], [63]	0.1	~8	Low	Medium	Medium
Ultrasound (Passive) [33], [63]	0.1	~2	Medium	Medium	Medium
mmWave (Active) [62], [64]	0.35	~2	low	Medium	Medium
mmWave (Passive) [65], [66]	0.098	~5	High	High	Medium
BLE [50], [67]	2.2m	~5	low	Medium	Medium

Table 3.1: Performance analysis for different indoor positioning technologies

3.6 Analysis

The detailed performance of each different positioning technology is summarized in Table 3.1. Referring to the table, it is obviously that the Wi-Fi based positioning technology has the advantage of low cost and high scalability as it can utilize the existing Wi-Fi infrastructure and function without any additional modification. However, it has a relatively high computational consumption which leads to a high complexity and a lower accuracy. On the other hand, high water-absorption also decreases the performance with the present human, which makes existing Wi-Fi based technology less practical for indoor localization applications.

IR-based positioning systems show higher accuracy than Wi-Fi. In comparison with other LIP methods, such as visible light, IR technology is less sensitive to ambient light condition, leading to an increase in adaptiveness [21]. However, the light-based nature largely affects its scalability, as IR signal cannot penetrate through wall and obstacles such as furniture, and the accuracy of IR-based systems is highly dependent on the overlap of FoV, the cost for this type of systems is also relatively higher. Similarly, as the RSSI-based solution is widely used in BLE-IPS, it also suffers from low scalability as many fixed transmitting devices are required to be deployed.

There are a number of common facts between ultrasound and mmWave technology. However, a wider bandwidth offers mmWave a better performance when handling multi-object scenarios, and the short wavelength also increases the accuracy as more antennas can be installed in the same area.

On the other hand, passive positioning methods are attracting more attention in recent years as the unobtrusive design enables the system to track untagged objects without disturbing the user, which requires less prior installation and knowledge from the user side. Moreover, as users can be anonymous in the passive system, the privacy is better protected.

In conclusion, the passive localization based on mmWave is the most recommended method that has a promising accuracy, scalability, and adaptiveness.

4 Localization Algorithm

The SLAM is a technique used to estimate a target's position while exploring or constructing a map of an unknown environment. The SLAM problem can split into two parts, the localization and the mapping. The localization refers to the process of knowing one's position in the environment, and the mapping means the process of knowing the features of the surrounding environment [38], [39].

To solve a SLAM problem, it requires one to find out the map (m) and a sequence of target's positions, *x*, (i.e., the movement trajectory):

$$x_{1:T} = \{x_1, x_2, \dots \dots, x_T\} \tag{4.1}$$

by processing a set of sensor observations, *z*, and odometry measurements, *u*:

$$z_{1:T} = \{z_1, z_2, \dots \dots, z_T\} \tag{4.2}$$

$$u_{1:T} = \{u_1, u_2, \dots \dots, u_T\} \tag{4.3}$$

The SLAM problem is always described as a probability problem due to the uncertainty introduced by the environment and the sensor, so the process of finding the map and trajectory can be treated as the estimation of posterior probability [68]. Therefore, the SLAM problem can be generally modelled as [69]:

$$p(x_{1:t}, m | z_{1:t}, u_{1:t}) = p(m | x_{1:t}, z_{1:t}) \cdot p(x_{1:t} | z_{1:t}, u_{1:t}) \tag{4.4}$$

The navigation of the environment could be done by inferring the location of the target and landmark of the environment through Equation 4.4. Basically, the possible position of the target (or the trajectory) is indicated by the odometry measuring and the observation, and the map could also be constructed by combining the observation with the built trajectory.

Based on the aforementioned statement, the SLAM problem can also be described as an optimization problem aimed to find the position of the target and landmark that best explains the observation within the distribution of uncertainty.

In the rest of this section, the different types of SLAM algorithms will be introduced based on their categories.

4.1 Filtering Based Algorithm

The filtering-based SLAM algorithms make use of observations and odometry information to estimate the posterior probability based on the Bayes theorem. The general methodology is to apply the guessing-and-correction cycle to predict the system. Based on the current location observation and odometry, upcoming target position can be estimated and then corrected by the environmental observation in the next iteration.

The Bayes Filter can be written as a two-steps process, thus the pose of the object (i.e. positions and orientation of the object, which a points that on the moving trajectory.), and the environment can be estimated and updated recursively:

$$\begin{aligned} bel(x_t) &= p(x_t|z_{1:t}, u_{1:t}) \\ &= \eta p(z_t|x_t) \int p(x_t|u_t, x_{t-1}) bel(x_{t-1}) dx_{t-1} \end{aligned} \tag{4.5}$$

where the η is the normalization constant, $bel(x_t)$ is the position of the current position, with the subscript t which means the current one.

Moreover, the Equation 4.5 can be separate into two parts, which are:

The prediction step:

$$\underline{bel}(x_t) = \int p(x_t|u_t, x_{t-1}) bel(x_{t-1}) dx_{t-1} \tag{4.6}$$

The Correction step:

$$bel(x_t) = \eta p(z_t|x_t)\, \underline{bel}(x_t) \tag{4.7}$$

The prediction step advances the previous estimation based on the odometry measurement, and the correction step uses the new observation obtained in the following iteration to correct the potential mistakes. In practice, the most common filters that used to solve the SLAM problem are Kalman Filter, Particle Filter, and their variant. Some typical filter-based SLAM algorithms will be introduced in the following subsections.

4.1.1 Kalman Filter

The Kalman Filter (KF) is a linear filter that can be considered as a subset of Bayes filter for solving the SLAM problem, it assuming the problem can be solved by a linear model and follows a Gaussian distribution assumption [70].

In KF, the trajectory and the observation are described as:

$$x_t = A_t x_{t-1} + B_t u_t + R_t \tag{4.8}$$

$$z_t = C_t x_t + Q_t \tag{4.9}$$

where R_t and Q_t are system parameters representing the uncertainty from the observations; the A_t is the state matrix that describes how the state evolves from time (t-1); B_t refers to the effect that the odometry u_t has to the pose change, and C_t is responsible for mapping a certain pose to the corresponding observation.

However, the application of KF is limited by the linear assumption and therefore unable to handle non-linear models that commonly happened in a SLAM problem. Therefore, the Extended Kalman Filter (EKF) is introduced to address the non-linear situation by a local linearization process through first-order Taylor Expansion [71], [72].

The motion model and observation model in EKF is:

$$x_t = g(u_t, x_{t-1}) + R_t \tag{4.10}$$

$$z_t = h(x_t) + Q_t \tag{4.11}$$

In comparison with Equation 4.8 and 4.9, the linear terms have change to the non-linear function g(·) and h(·) . After the first order Taylor Expansion, these two functions are described as follows:

$$g(u_t, x_{t-1}) \approx g(u_t, \mu_{t-1}) + \frac{\partial g(u_t, \mu_{t-1})}{\partial x_{t-1}}(x_{t-1} - \mu_{t-1}) \tag{4.12}$$

$$h(x_t) \approx h(\underline{\mu}) + \frac{\partial h(\underline{\mu}_t)}{\partial x_t}(x_t - \mu_t) \tag{4.13}$$

where the terms $\frac{\partial g(u_t, \mu_{t-1})}{\partial x_{t-1}}$ and $\frac{\partial h(\underline{\mu}_t)}{\partial x_t}$ is the Jacobian, the matrix of partial derivatives, that also refer to G and H.

From the view of implementation, the process of positioning and mapping can be done through several steps which cooperate with the aforementioned EKF motion and observation model together [72].

The first two steps involve calculating of the predict mean, $\underline{\mu}_t$, which represents the expected position of the following movement, and the predict covariance, $\underline{\sum}_t$, which illustrate the uncertainty:

$$\underline{\mu}_t = g(u_t, \mu_{t-1}) \tag{4.14}$$

$$\underline{\sum}_t = G_t \sum_{t-1} G_t^T + R_t \tag{4.15}$$

Those two steps demonstrate how the prediction involves given the odometry measurement, u, where μ_{t-1} represent the previous mean, the estimated position that has been corrected at time t-1.

On the other hand, after the prediction of the up-coming position and the corresponding uncertainty, the next step of the EKF process is to correct the expected value through the comparison between the prediction and actual measurement:

$$K_t = \underline{\sum}_t H_t^T (H_t \underline{\sum}_t H_t^T + Q_t)^{-1} \tag{4.16}$$

$$\mu_t = \underline{\mu}_t + K_t(z_t - h(\underline{\mu}_t)) \tag{4.17}$$

$$\sum_t = (I - K_t H_t) \underline{\sum}_t \tag{4.18}$$

In the correction process, the first step is calculating the weighting factor, the Kalman Gain, which indicates how solid the prediction is. Furthermore, the belief of the position, $\mu_t$is produced based on the difference between the actual measurement and prediction primarily. The last calculated value is the covariance, $\sum_t$, which helps with the estimation of new $\underline{\sum}_t$ value in Equation 4.15.

In practice, the prediction and correction process will be executed iteratively to build up the map target trajectory and landmark.

4.1.2 Particle Filter

The Particle Filter (PF) is another subset of Bayes Filter which estimates the posterior probability by particles [73]. In PF, the probability distribution function can be represented as a set of particles that own one set of state variables, and the probability approximating is processed through the collection of those guess sets.

For each particle set, it contains the state hypothesis (x), the corresponding weight (ω), and total amount of the particle (t).

$$\chi = \{(x^j, \omega^j)\}_{j=1:t} \tag{4.19}$$

And the state of the target contains at least three information, which are the x and y position and the orientation of it [74].

Therefore, the probability representation of the sample sets is the sum of all the particles with its weight:

$$p(x) = \sum_{j=1}^{J} \omega^{[j]} \delta_{x[j]}(x) \tag{4.20}$$

The procedure of PF is also composed of the prediction and update stage, but it has a special process called re-sampling which samples the particles again.

In PF, the process of drawing a proposed particle set can be seen as the prediction step [75]:

$$x_t^j \cong p(x_t | x_{t-1}, u_t) \tag{4.21}$$

And the correction process is:

$$\omega_t^j \propto p(z_t | x_t, m) \tag{4.22}$$

Similar to the EKF, motion and observation model is required to deal with the prediction and correction process. The motion of the robot will be model in the view of velocity information:

$$x_t^j = (x_t\ y_t\ \theta_t\ ) = (x_{t-1}\ y_{t-1}\ \theta_{t-1}\ ) + \left(-\frac{v}{\omega} sin\ sin\ \theta\ + \frac{v}{\omega} sin\ sin\ (\theta + \omega\Delta t)\ \ \frac{v}{\omega} cos\ cos\ \theta\ - \frac{v}{\omega} cos\ cos\ (\theta + \omega\Delta t)\ \ \omega\Delta t\ \right) \tag{4.23}$$

where a single sample,x_t^j, repersent the particle j generated at time t. It contains at least three element, which x, y, θ signifies the 2-D position and orientation of the target, and v and ω indicate the translation velocity and rotational velocity.

In PF, the adjustment of the predicted pose is completed through the weight factor, and this step always involve the comparison between the computational value and the measured value. Therefore, the observation model can be expressed as [75], [76] :

$$\omega_t^j = \frac{p(x_t^i)}{\pi(x_t^i)} = \omega_{t-1}^i \cdot e^{\frac{match^i}{f}} \tag{4.24}$$

Accordingly, the p(·) and π(·) are the target and proposal distribution, the ω_{t-1}^i means the previous weight, the match resulting by the comparison between the local map and global map, and f reflect the weight's distribution.

The process of the one complete iteration for the incremental localization and mapping through particle filter is composed of five steps [74], [76]:

The first step is initialization which setup N predicted sample set, or the initial guess, and each of them owns a weight of 1/N. The second step is the sampling process, the particles from the motion model is taken as sample from the proposed distribution, sample from $\pi(x_t)$, and the particle is generated based on that. After this, the particle weight will be calculated based on Equation 4.24, and the resampling process is taken for filter out those particles that not significant. The threshold is calculated as:

$$Threshold\ = \frac{1}{\sum_{i=1}^{N}\ (\widetilde{\omega^i})^{\ 2}} \tag{4.25}$$

where N is the number of the sample.

The last step is updating those new particles and repeat the whole process, which similar to the KF.

4.2 Smoothing Algorithm

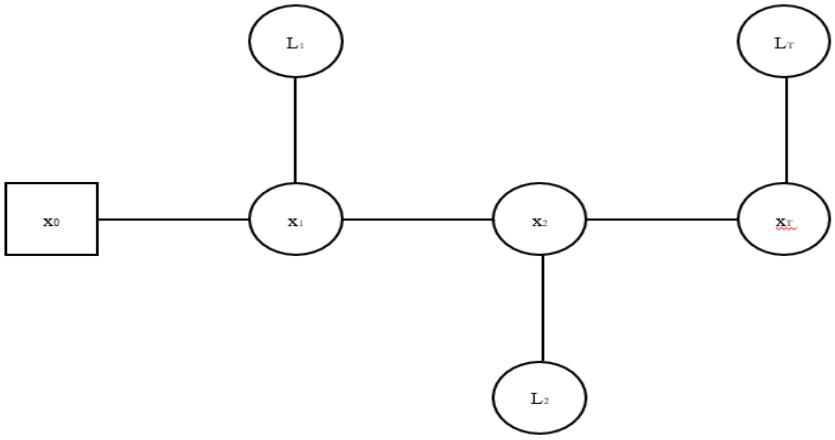

Figure 4.1: Example of Factor Graph

The smoothing SLAM algorithm also commonly referred to as full SLAM which analyses the entire target's trajectory, this method is characterized as an offline solution and directly reflecting the target's trajectory and the measuring of the landmark by constructing the graphical model [43].

The graph construction is constructing a map of the environment based on the sensor measurement, and the graph optimization is determining the configuration of poses and edges of the graph. This kind of method can be represented by a network graph as indicated in Figure 4.1 [77]. In this graph, the circled and square symbols are referred to as a variable that indicates the location, and the edges connecting those variables are factors that constrain those variables by related measurement. More specifically, variables labeled with x are modeling the pose of the target, and L is the position of the landmark. Moreover, the factors that connect two poses (x) can be referred to as the odometry, otherwise, it could be called an observation if it is connecting a pose to the landmark (L).

In the earlier implementation, the graph-based SLAM technologies are mainly used to address the challenge of full SLAM, which is to analysis the whole trajectory in an offline mode. However, in recent years, the incremental graph SLAM algorithm is becoming more attractive as the online method is more effective and useful in solving SLAM problems in real-time [73]. Therefore, our research will primarily focus on the incremental graph algorithm.

In the rest of this chapter, two different smoothing SLAM algorithm will in introduced and discussed in detail.

4.2.1 Iterative Least Square

This graph-based approach uses a probabilistic model theory that offers a graphical optimization to solve the SLAM problem utilizing non-linear square method [78]. This method converts pose estimation and sensor observation into nodes and edges, which means constructing a graph with nodes that represent the pose of the target or landmarks and edges that show the spatial constrains connecting two poses or pose and landmark [79]. Each node consists of the sensor measurement acquired at a corresponding location, and edges formed by odometry measurement or the observation matching between two consecutive nodes [77]. However, the observation model is multi-modal which can conduct multiple possible edges through a single observation. This means the connectivity between two nodes can be represented by a non-Gaussian probability distribution. As a result, the critical problem is estimating the constraint, in which adding the factors to the graph, and the process also known as data association.

This section is mostly focused on the back-end map optimization, and the goal of it is to estimate a state that best fit the measurement that explains the constraint, in other words, to minimize the difference between the observation and estimation.

The goal of the graph-based SLAM problem is to find the most likely pose and edge configuration with minimal difference between the prediction and the actual measurement. The error can be computed as follows:

$$e_{ij} = z_{ij} - f\left(x_i, x_j\right) \tag{4.26}$$

As the error of a measurement depends only on the state and is a scalar.

$$F_{ij}(x) = e_{ij}(x)^T \Omega_{ij} \cdot e_{ij}(x) \tag{4.27}$$

where the F(x) is the log likelihood, Ω is the information matrix that represents the uncertainty of the individual measurement, which means the weight of each trial.

The process is to find the maximum likelihood trajectory based on the observations and can also be considered as finding the configuration of nodes x^* and edges that minimize the non-linear error equation by solving the lest-square problem:

$$x^* = F(x) \tag{4.28}$$

$$x^* = \sum e_{ij}(x)^T \Omega_{ij} \cdot e_{ij}(x) \tag{4.29}$$

The cumulation of the error is a non-linear process, and the optimization problem can be solved by a local iterative process with the following steps:

a) Local linearization for the non-linear error function around the current solution
b) Work out the first derivative of the local linear error function.
c) Find the minimum value of the derivative function.
d) Introduce new sampling.
e) Repeat

In a word, this is a graph-based algorithm that convert SLAM problem into the posterior probability estimation through the expression in Bayes Network. Moreover, the maximum posterior probability can also be expressed by least square problem and solved by interactive Gaussian-Newton method.

4.2.2 iSAM2

In the iSAM2 algorithm, the factor graph is used to describe the SLAM problem, and it solves the SLAM problem by matrix factorization, and builds up the graphical model of Bayes tree by factor elimination [80], [81].

In this case, the SLAM problem can be represented by a factor graph. In general, a variable is equivalent to the vertices, or the variable illustrated on the Figure 4.1, and the factors can be seen as the edges. The factorization of function f (Θ) can be shown as:

$$f\ (\Theta)\ = \prod_i\ f_i(\Theta_i) \tag{4.30}$$

where the Θ_i is a set of variables which near to the factor f_i.

Based on Equation 4.30, the factor graph can be seen as the product of all the factors on the graph. The SLAM problem could also be described as maximization problem:

$$\Theta^* = \arg\max_{\Theta} f(\Theta) \tag{4.31}$$

where Θ^* is the variable assignment.

On the other hand, Equation 4.31 can be converted to the expression of a minimization problem:

$$\Theta^* = \arg\min_{\Theta} \left(-\log(f(\Theta)) \right) \tag{4.32}$$

Moreover, the iSAM2 is modeling the measurement as a Gaussian function, by substituting the Gaussian model into Equation 4.32, the following expression could be obtained [80]:

$$\Theta^* = \arg\min_{\Theta} \frac{1}{2} \sum_i ||h_i(\Theta_i) - z_i||^2_{\Sigma_i} \tag{4.33}$$

The Equation 4.33 is showing how the problem could be solved by the non-linear least-square way, where the $h_i(\Theta_i)$ is the measurement function and the z_i is the measurement, and the $\sum$ is the covariance matrix.

The Equation 4.33 could be solved non-linear optimizer, and the linearization process will be performed at each iteration of the iSAM2 to obtain a linear approximation of it.

The first step of iSAM is the variable elimination by removing all the factors that link to the target, $f(\Theta_i)$, and define the separator S, which the variables that directly adjected with it. Then, a joint density $f_{joint}(\theta_j, S_j)$ is defined where the θ refers to the eliminated variable [80]. For instance, in Figure 4.1, if the variable L_1 is be eliminated, then it could be expressed as $f_{joint}(L_1, X_1)$

After the elimination of all variable, a Bayes net could be defined with the density:

$$P(\Theta) = \prod_j f_j(\Theta_j) = \prod_j P(\theta_j | S_j) \tag{4.34}$$

Then, the Bayes tree can be constructed based on each conditional density $P(\theta_j|S_j)$ in the Bayes net, and those nodes will be processed with a reversed order compared to the elimination, which has shown in Figure 4.2.

For each conditional density $P(\theta_j|S_j)$ of the Bayes net, in *reverse* elimination order:
If no parent ($S_j = \{\}$)
    start a new root clique F_r containing θ_j
else
    identify parent clique C_p that contains the first eliminated variable of S_j as a frontal variable
    if nodes $F_p \cup S_p$ of parent clique C_p are equal to separator nodes S_j of conditional
        insert conditional into clique C_p
    else
        start new clique C' as child of C_p containing θ_j

Figure 4.2:The Algorithm of Creating a Bayes Tree [80]

For those conditional densities that have an empty separator, their variable θ will be contained in a new root clique F_r. Otherwise, the parent clique C_p is defined as a clique that contains a frontal variable, F, which is also the first eliminated variable in the separator. After that, the result of the comparison between the union of frontal F_p and separator S_p of the parent clique C_p, and the separator S_j of the conditional is obtained. If they are equals, then the conditional will insert to the clique C_p, or the conditional density will send to a child clique of C_p.

For updating the Bayes Tree with the new factors, the first step is removing all the cliques that are affected by the factor, corresponding parent clique, and the root, then re-interpret it to the factor graph. Secondly, the new factor will be insert to the factor graph, after the re-order of the variable, the factor elimination and Bayes Tree construing is preformed again. Also, the incremental process of updating the Bayes Tree is only applied locally. This means that if a new measurement f (x_i, x_j) is added, only the subtrees that contain x_i and x_j and its root will be affected, but not the whole Bayes Tree, other parts of the Bayes tree remain unchanged. For the affected part, the changes will be handled in the original factor graph, and the variable elimination and tree constructing process that mentioned before is performed. Eventually, the remaining sub-trees are reattached to form the new Bayes tree.

Moreover, the iSAM2 also performed a fluid relinearization, which is used to handle updates of non-linear data, which can simply be explained as performed relinearzation only when needed. This process involves three steps, the first step is marking all the current updating value that above a threshold. The second step is updating the linearization point:

$$\Theta_j := \Theta_j \oplus \Delta_j \tag{4.35}$$

where the Δ_j us the current updating value, and Θ_j is the localization point, and the last step is marking all clique which involving to the Θ_j.

Therefore, one single iSAM2 processing can be described as:

1. Add the new factors.
2. Initialize any new variable and add the new variables.
3. Fluid linearization as mentioned.
4. Re-estimate the top of Bayes tree with the process of updating non-linear factor.

5. For each clique from the root, compute the update Δ_k from the local conditional density. Then determine those variables in Δ_k that changes more than the threshold, and recursively process each descendant containing such variable.
6. Updating the current estimation.

4.3 Comparison

For filter-based algorithms, the KF is suffering from the lack of ability to handle non-linear situations, and the limitation from Gaussian assumption.

According to [82], the pose estimation by EKF illustrates an observably linear feature and diverges from the real measurement at the turning point, which means the error accumulation in EKF has significant boost in higher order models. Even the study also indicated that EKF can produce a steady output when mapping the environment, but it still has a slightly higher root mean square (RMS) error compare with PF [83].

In comparison, the graph-based approach shows the potential that has better accuracy than the PF-based approach as the error accumulation is slower than PF [84]. The greatest advantage of PF is that it eliminates the process of Jacobian calculation, which is computationally expensive. However, graph-based SLAM approaches show similar potential, and the nature of graph-SLAM make it relatively memory efficient than filter-based method [85]. Among all the graph-based approaches, the iSAM2 algorithm is one of the best options that can avoid complex calculation as it expresses the problem as Bayes tree rather than in matrix form. The nature of the Bayes tree makes the new measurement that comes into the system makes a limited effect on the existing graphical structure, and only a small part needs to be modified. This mean iSAM2 do not required repeat the whole process step for every increment like other mentioned algorithm, but only locally redo the estimation process. While iSAM2 is still limited by the Gaussian assumption, it has demonstrated promising accuracy in [81].

5 Radar Sensor

To obtain position information, certain sensor such as a camera or radar needs to be used to sense the world. The radar is a detection system designed for exploring the information of obstacles presented within its functioning range. It is a rangefinder system that is widely deployed around the world and can be separated from other similar systems like lidar or sonar as it transmits radio signals. It offers good accuracy and is immune to light condition [86].

Fundamentally, a radar system should contain two parts, which are the transmitter and receiver. A transmitter is responsible for generating certain radio waves to the physical environment. The receiver is an antenna that is used to sense the signal that reflects from the obstacle or the echo signal. Moreover, the receiving end is also responsible for revealing and analyzing the echo signal, and the result will be used to estimate the angle and distance of an obstacle depending on the type of signal that the system used. Ideally, the distance and the angle of the object could be workout by sampling the time delay or phase difference between the transmitted signal and the echo signal.

In this thesis, IWR1443 mmWave sensor module developed by Texas Instruments is used and hence the mmWave radar discussion in the following sections will be based on the IWR1443 sensor. It is a frequency modulated continuous wave (FMCW) based mmWave sensor and operates between 76 to 81 GHz bandwidth [46]. The detail of the radar module will be discussed in the later of this chapter.

5.1 FMCW Radar

The FMCW is a signal modulation method that changing the signal frequency while it working. Rather than pulses, FMCW radar transmits a continuous modulated sinusoidal wave, this could reduce the signal overlap caused by the echo on the returning and could be helpful especially in indoor environment [86]. Moreover, the frequency modulation also leads to a simpler signal processing compared to the modulating in temporal.

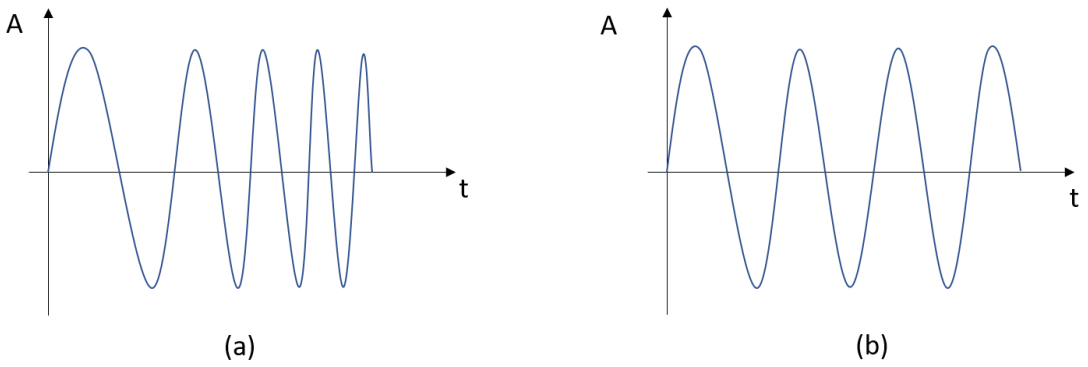

Figure 5.1: Example of FMCW in time

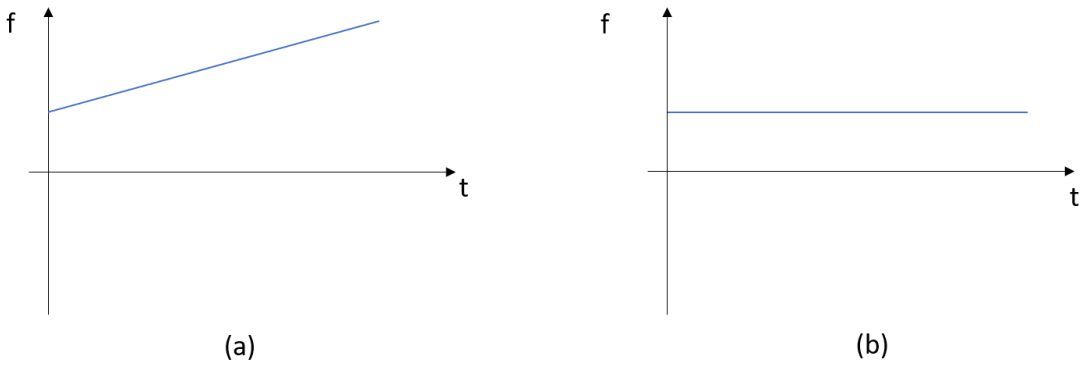

Figure 5.2: Example of FMCW in frequency

In FMCW modulation, a sinusoidal wave that experiences a complete cycle of frequency increment is considered as a "chirp". Referring to Figure 5.1(a) and 5.2(a) illustrate how the FMCW signal behaves in both time and frequency domain in comparison with a standard sinusoidal wave (i.e. without any modulation) in Figure 5.1(b) and 5.2(b). In practice, the increment process iterative, and changes the frequency from the minimum to the maximum and then return to the minimum for the next sweeping cycle.

For IWR1443, one chirp refers to a signal that has a linearly increased frequency from 77GHz to 81GHz as it has a 4GHz bandwidth. The signal has a period of 40us and the rate of increase is at 100MHz/us [46].

On the receiving end, the received signal will be fed into a mixer along with the instantaneous FMCW signal from the transmitter to estimate the distance of the object. This process is shown in Figure 5.3, the Synth is a synthesizer that generates the "chirp" signal which will be emitted by the transmitter, TX. The received signal will be compared with the instantaneous signal generated by the synthesizer to work out the distance, in which, the mixer is helping to find the frequency and phase difference.

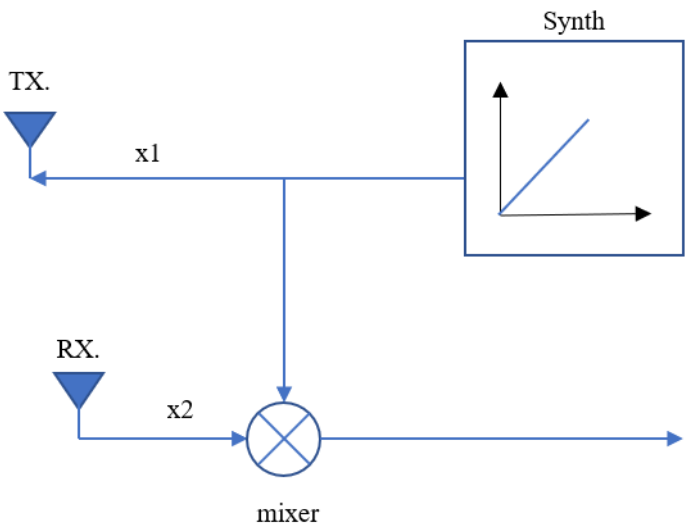

Figure 5.3: FMCW radar block diagram

Mathematically, the transmitted signal x1, and the echo signal x2 can be modeled as:

$$x1 = \sin(\omega_1 t + \phi_1) \tag{5.1}$$

$$x2 = \sin(\omega_2 t + \phi_2) \tag{5.2}$$

Then, the output of the mixer will be:

$$x_{out} = \sin[(\omega_1 - \omega_2)t + (\phi_1 - \phi_2)] \tag{5.3}$$

The operation of finding x_{out} is also corresponding to generating the intermedia frequency, the IF signal,

For instance, assuming there is only one obstacle in front of the radar, the x1 and x2 can be expressed as shown in Figure 5.4 below.

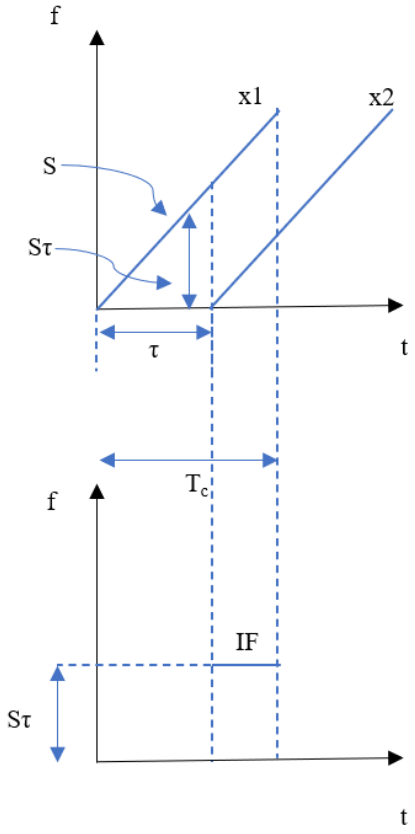

Figure 5.4: Example of IF signal

As shown in Figure 5.4, the echo signal will have a delay to the x1 caused by the round-trip-time τ of the reflection, and the slope of the frequency increase is S.

When the echo signal is received, it will be sent to the mixer and multiplied with the instantaneous signal, x1, generate by the synthesizer, and by applying FFT to it, the process will finally result in an IF signal which:

$$IF = S\tau \tag{5.4}$$

where the S is the rate of frequency change, and τ is the round-trip time that can be represent as:

$$\tau = \frac{2R}{c} \tag{5.5}$$

where the R is the distance between the radar and the obstacle, and c is the speed of light.

From Equations 5.4 and 5.5, it is clear that the IF signal is proportional to *R*, which is the distance between the object and radar. Also, based on the concept discussed above, the number of IF signals are

also positively related to the number of obstacles sensed. For instance, if there are three objects sensed by the radar, there will be three IF signals generated by the mixer, and each of them will have a value corresponding to the distance to an obstacle.

5.2 IWR1443

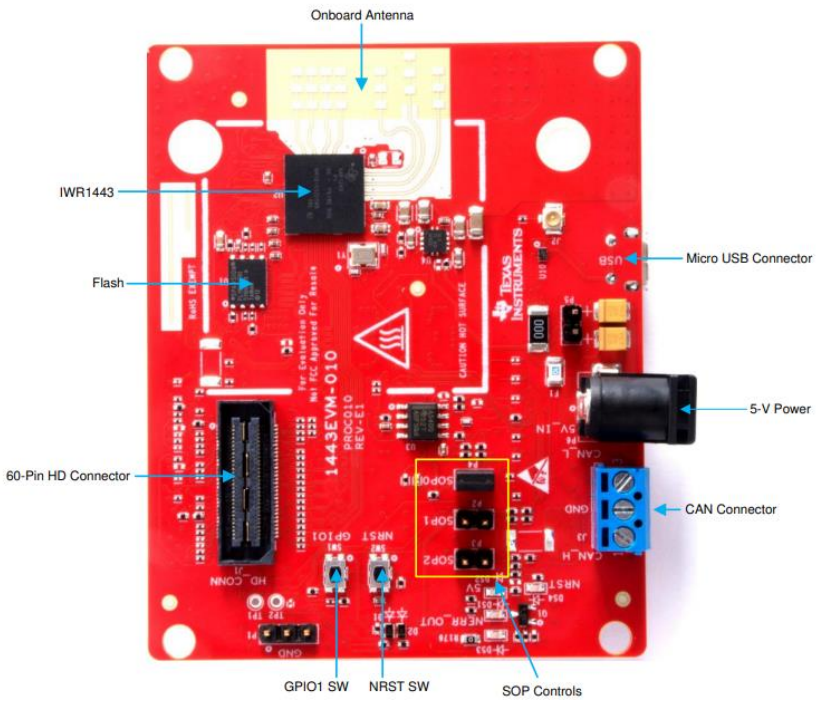

Figure 5.5: IWR1443 Front View [46]

The IWR1443 has an antennas array with 3 transmitters and 4 receivers, and this array allows to sense multiple objects and the elevation. With this array, the IWR1443 sensor features a 100-degree Azimuth FoV with 15-degree resolution, and a 30-degree resolution in the elevation plane.

The processing chain of this radar device is illustrated in Figure 5.6.

Figure 5.6: IWR1443 Processing Chain

Referring to Figure 5.6, it contains the processing steps based on the components provided by the IWR1443 SDK, and the processing components from custom application code. Within the SDK, after

the data input is captured, an FFT on first dimension is performed to estimate the range between the object and the radar After this, the second FFT is performed on a different dimension to extract the doppler information.

In IWR1443, the Constant False Alarm Rate (CFAR) theory is used, it is a technique that helps to distinguish the amplified and converted signal from the echo (i.e. the IF signal) from the background noise. In the process chain, the CFAR step filters out signals that have power less than a threshold value [87]. This step also determines the number of obstacles sensed within a frame. In the same frame, the larger the CFAR threshold, the less obstacle tends to be detected by the system, and vice-versa.

For the angle estimation, multiple antennas will be involved to perform the AoA computation.

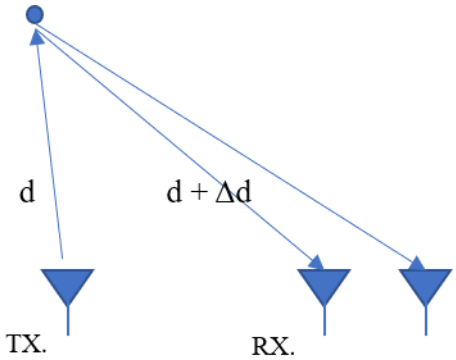

Figure 5.7: Obstacle Detection

Assuming a setup with two receiving antennas as shown in Figure 5.7, the distance of the echo signal that traveled from the obstacle to the receiver can be labeled as d, and the distance to an adjacent receiver is d + Δd. The difference in distance will also result in a phase change, which could be modeled as:

$$\omega = \frac{2\pi \Delta d}{\lambda} \tag{5.6}$$

$$\omega = \frac{2\pi d \sin\theta}{\lambda} \tag{5.7}$$

By rearrange the formular, the equation for obtain the angle can be seen as:

$$\theta = sin^{-1}\frac{\lambda\omega}{2\pi d} \tag{5.8}$$

where λ is the wavelength of the signal, ω is the phase difference, and d is the distance between the object and radar

Considering the 3D beamforming operation, the angular position of the obstacle is a composite of the azimuth and elevation component. For IWR1443, the azimuth plane has 4 receiving antennas that work with 2 transmitting antennas, and hence result in 8 virtual antennas in total:

$$r = A_1 e^{j\psi}[1e^{j\omega_x}e^{j2\omega_x}e^{j3\omega_x}e^{j4\omega_x}e^{j5\omega_x}e^{j6\omega_x}e^{j7\omega_x}] \tag{5.9}$$

where A is the amplitude, ψ representing the initial phase, and ω_x is the phase difference among each antenna.

Similarly, for the elevation plane, there are 4 receiving antennas working with 1 transmitting antenna, which result in 4 virtual antennas:

$$r = A_2\, e^{j(\psi+2\omega_x-\omega_z)}[1e^{j\omega_x}e^{j2\omega_x}] \tag{5.10}$$

where ω_z is the phase difference between azimuth and the corresponding elevation of the antenna above the azimuth plane, which is caused by and represent in the antenna array shown below:

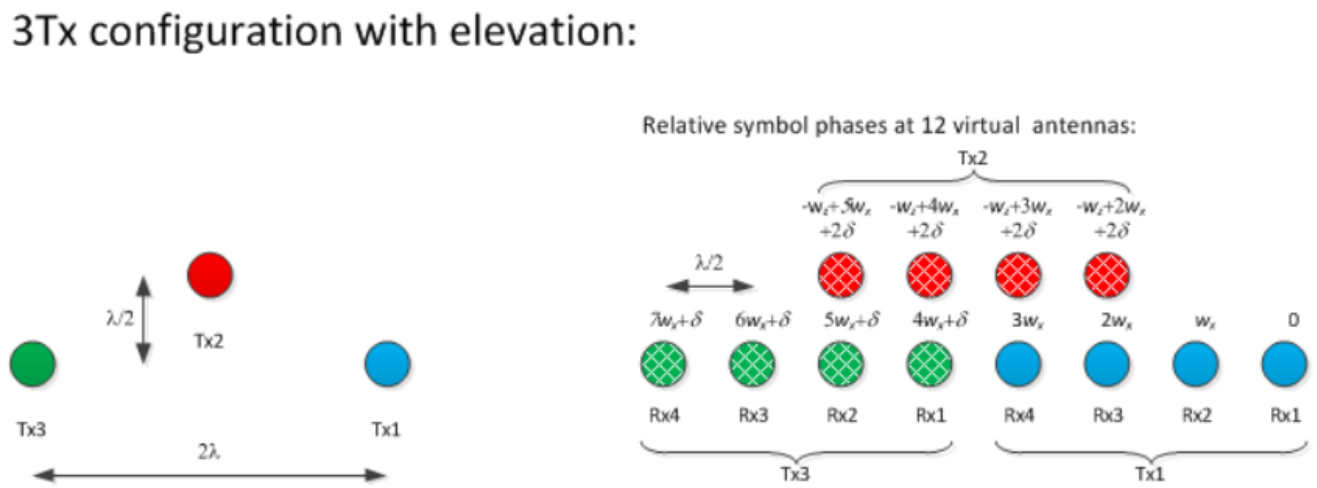

Figure 5.8: Antenna Array [88]

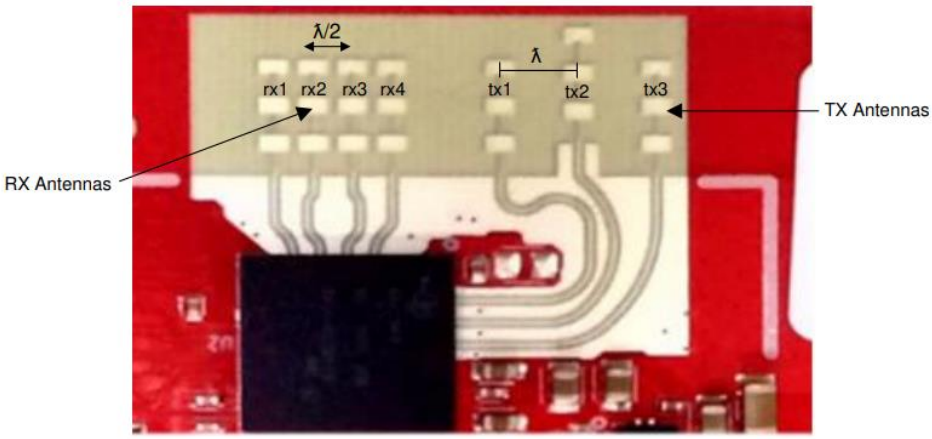

Figure 5.9: PCB Antenna [46]

The Figures 5.8 and 5.9 is showing the antenna array of the IWR1443, and what its looks like on the board. In practice, TX2 can be used to measure the elevation angle.

Equations 5.9 and 5.10 is showing the azimuth and elevation component of the echo signal respectively, and after the process of the FFT competed by the previous stage, the IF value can be calculated using the peak P_1 calculated from the azimuth plane and peak P_2 calculated from the elevation plane.

$$P_1 = A_1 e^{j\psi} \tag{5.11}$$

$$P_2 = A_2\, e^{j(\psi+2\omega_x-\omega_z)} \tag{5.12}$$

The phase difference along the azimuth plane, ω_x, can be expressed as:

$$\omega_x = \frac{2\pi}{N} K_{MAX} \tag{5.13}$$

where N is the number of virtual antennas, and K_{MAX} is the index of the peak in log magnitude FFT, which in range of $[-\frac{N}{2}, \frac{N}{2} - 1]$ [88].

For calculating the phase difference between azimuth and the corresponding elevation plane, firstly should get the P_1 and P_2 multiplied:

$$P_1 \cdot P_2^* = A_1 A_2 e^{j(\psi-(\psi+2\omega_x-\omega_z))} \tag{5.14}$$

$$\omega_z = \angle(P_1 \cdot P_2^* \cdot e^{j2\omega_x}) \tag{5.15}$$

For now, the range can be calculated by:

$$R = k_r \frac{c \cdot F_{SAMP}}{2 \cdot S \cdot N_{FFT}} \tag{5.16}$$

where k_r is a range index, c is the speed of light, F_{SAMP} is the sampling frequency, N_{FFT} is the 1D FFT size.

Based on Equation 5.16, the position of the detected object in a 3D Euclidean space can be calculated as follows:

$$x = R\cos(\phi)\sin(\theta) = R\frac{\omega_x}{\pi} \tag{5.17}$$

$$z = R\sin(\phi) = R\frac{\omega_{xz}}{\pi} \tag{5.18}$$

$$y = \sqrt{R^2 - x^2 - z^2} \tag{5.19}$$

where the ϕ and θ is representing the angle at different plane as shown in Figure 5.10, ω_x and ω_z phase difference illustrates in Figure 5.8.

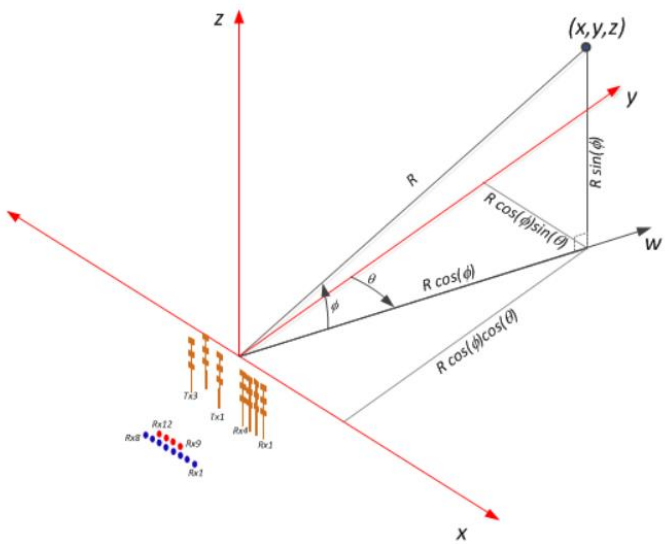

Figure 5.10: Coordinate Geometry of IWR1443 [88]

In practice, the result, the position of the sensed object, is usually transmitted to the computation device for a further data processing. Similar in this positioning system, the data from the radar device will be

the input for both ICP and iSAM2 algorithm.

The data structure of IWR1443 can be sent to the host computer via the UART protocol, which contains a 36 bytes header, an 8 bytes TLV header, the group of information about the detected object with varying size depending on the number of objects, a 32 bytes statistic profile and 0-31 bytes padding bytes.

The header contains the following data group:

- Magic Word: A fixed 8 bytes sync word.
- Version: The SDK version of the used device.
- Total Packet Length: Indicates the total packet length of the current input frame.
- Device Type: IWR1443 in this case.
- Frame Number: The number of frame that be transmitted within this packet.
- Time: The CPU time when the message was created.
- Number of Detected Obstacles
- Number of TLVs: The number of groups of data.

The header is followed by the TLV header that indicates the type of information contained in the following message and the payload length.

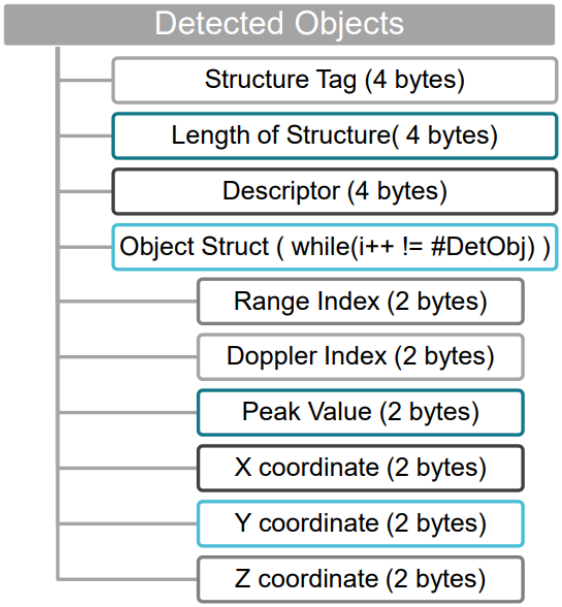

Figure 5.11: Detected Objects Data Structure [95]

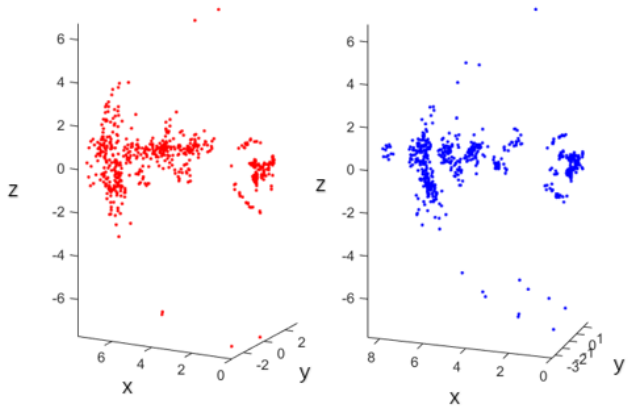

Figure 5.12: Example of IWR1143 Output Data

The Detected Object is also a complex data structure as illustrated in Fig. 16. The Descriptor contains the sequence number of the currently reading object, and the Q Formatting information if the X, Y and Z value. Overall, the data comes from the IWR1443 to the host computer is a point cloud data of the sensed environment. The example of two continuous IWR1443 data output frame is shown in Figure 5.12.

6 ICP Algorithm

As discussed in the previous section, the SLAM problem can be separated into mapping and localizing problems, which involve the steps of sensing and mapping the physical world and being aware of one's position. While mmWave radar can be naturally applied to map the surrounding environment, some extra steps are necessary to estimate the target trajectory (i.e. localize). Typically, IMU is a popular solution to be fused with other positioning technologies including mmWave to achieve better localization accuracy [89]–[91], However, it suffers from disadvantages, such as extra hardware units will be required, the error accumulation, and the data alignment problem. Therefore, a novel approach is proposed in this research to use only mmWave radar to achieve both mapping and localizing.

In this research, the ICP algorithm is used as a replacement for the IMU to measure the target's movement. It is a dominating algorithm in the aspect of aligning three-dimensional models and is first proposed in 1992 [92]. The process of alignment is about estimating a relative rigid-body transformation by minimizing the error metric of a pair of corresponding points on two related data sets [45]. The ICP algorithm is commonly applied to point cloud data sets which are the outputs generated by the mmWave radar. The process of alignment can be used to infer the location and orientation change, which allows the use of mmWave radar data to trace target trajectories without using an IMU. In general, the ICP algorithm is an iterative algorithm and each iteration is performed between two consecutive data sets (e.g., two frames of point cloud data points). One of the data sets is treated as the geometric reference, and the other input data set that is to be aligned to the reference is called reading, this can be expressed as:

$$^{P}T_{Q} = \arg\min(\mathrm{e}(\mathrm{T}(\mathrm{P}), \mathrm{Q})) \tag{6.1}$$

Where the P is reading, and Q is reference. The $^{P}T_{Q}$ is the transformation that can minimize the error function e (P, Q), and the T(P) refers to the transformation applied to the input reading.

Moreover, the error function is an equation of the matching function, which is responsible for associating the points pair between the reference and the reading. It equals the sum of an outlier rejection function values the influence that each point-matching took, and a distance function to work out the geometric distance between selected points.

$$e(P, Q) = \sum_{(p,q)\in M} w(p, q)d(p, q) \tag{6.2}$$

$$M = match(P, Q) = \{(p, q): p \in P, q \in Q\} \tag{6.3}$$

$$W = outlier\ (M) = \{w(p, q): \forall(\mathrm{p}, \mathrm{q}) \in M\} \tag{6.4}$$

where M is the matching function, W, or *w(p, q)*, is the outlier rejection function, and *d(p, q)* is distance function, . In another word, the minimum transformation that can best align the reading point cloud and the reference point cloud is calculated through the error function, which sums all the distance of correlating points with its weight.

More specifically, those process can be separated into five stages, namely selection, matching, weighting, rejection, and minimizing, which will be explained in more details in the following paragraphs.

In the selection stage, one or some of the points are selected for matching in both data sets. There could be some selecting strategy that is used to improve the accuracy. A random selection can be considered as one of the most basic point selecting methods, which will randomly choose the point pairs for each iteration, so the effect caused by the outlier value will be reduced [93].
The matching stage aims to work out the correlation of those selected points. It is a process that approaches the reading point cloud to the reference point cloud. In the most direct way, the distance between the selected point with all of its near neighbors will be calculated, and the shortest one will be kept. However, the nearest-neighbors-based method may also lead to a mismatch when the curvature exists in the model data. Alternatively, as a complement to the uncertainty caused by curvature, the line-surface intersection technique can be used
[93]. It can also be referred as normal shooting, in which the data point is paired to the surface intersection indicated in the selection phase. The difference between those mentioned method could be shown as Figure 6.1, which indicates the miss-matching for the nearest neighbor method, and how the normal shooting performance under the same condition.

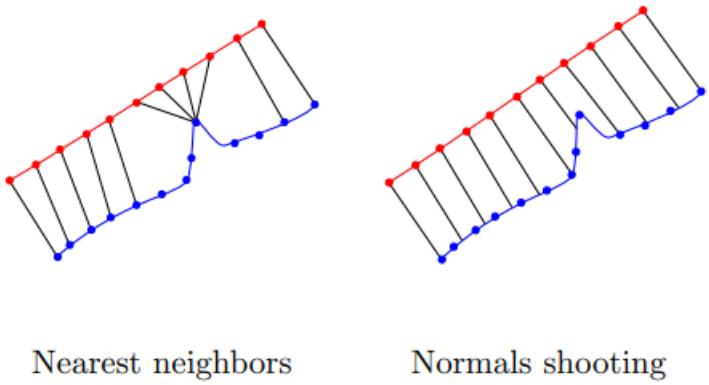

Figure 6.1: Nearest Neighbors vs Normal Shooting

In each iteration, it is impossible to have the data and model cloud point to perfectly match as there exist outliers, and the radar movement will also result in the shift of the sampled points. Therefore, the weighting stage is to evaluate the influence of each pair of matched points. As described in Equation 6.4, the weight could be calculated to evaluate the importance of the matching pairs. For instance, other researchers have suggested that the importance of a point pair could be worked out by the distance between two points [94]:

$$\omega = 1 - \frac{dist\ (p, q)}{dist_{MAX}} \tag{6.5}$$

After weighting, the rejection stage is used to eliminate those point pairs which do not fit the criteria.

Moreover, the minimization is performed at the last step, as mentioned in Equation 6.1, the transformation that could minimize the difference between the reading and reference is required to be detected. This process could be modeled as:

$$E = \sum \|Rp + T - q\|^2 \tag{6.6}$$

where R is the rotation, T is the translation, p and q is the reading and reference respectively.

The ICP algorithm will finally output a rotation matrix and translation vector that best fitted the reading point cloud to the reference point cloud. Where the rotational matrix is the combination of the rotation in x, y and z direction, as shown in Equation 6.7 to 6.10.

$$R_x(\alpha) = \begin{bmatrix} 1 & 0 & 0 \\ 0 & \cos(\alpha) & -\sin(\alpha) \\ 0 & \sin(\alpha) & \cos(\alpha) \end{bmatrix} \tag{6.7}$$

$$R_y(\beta) = \begin{bmatrix} \cos(\beta) & 0 & \sin(\beta) \\ 0 & 1 & 0 \\ -\sin(\beta) & 0 & \cos(\beta) \end{bmatrix} \tag{6.8}$$

$$R_z(\gamma) = \begin{bmatrix} \cos(\gamma) & -\sin(\gamma) & 0 \\ \sin(\gamma) & \cos(\gamma) & 0 \\ 0 & 0 & 1 \end{bmatrix} \tag{6.9}$$

$$R_{\alpha\beta\gamma} = R_z(\gamma)R_y(\beta)R_x(\alpha) \tag{6.10}$$

Where the α, β, and γ are the rotation respect to x, y, and z axis respectively, and the translation vector is indicating the displacement:

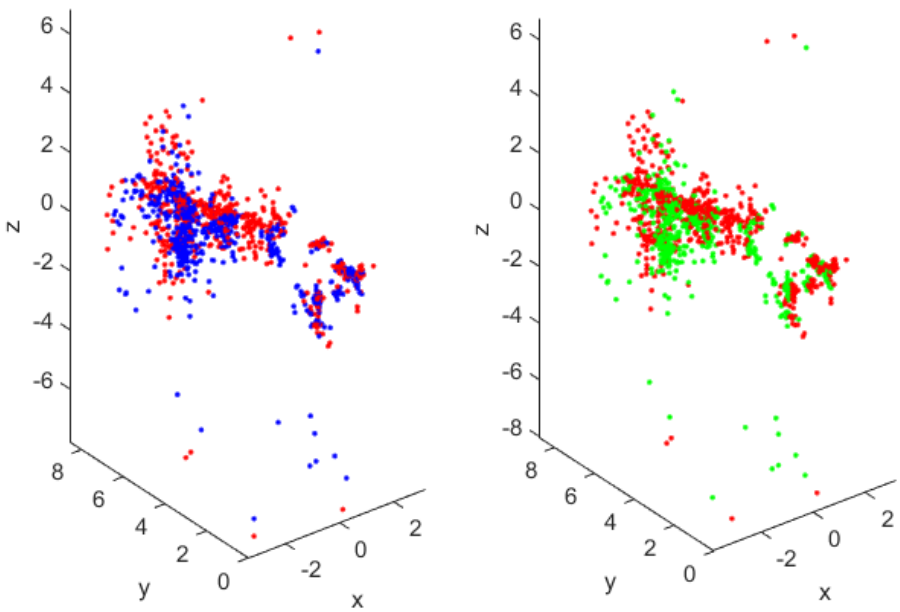

$$T = \begin{bmatrix} x \\ y \\ z \end{bmatrix} \tag{6.11}$$

Figure 6.2: Example of ICP result

Figure 6.2 is showing an example of ICP result, where the blue points are referring the data point, red points refer to the model points, and the green points are the data point after the application of the ICP result.

7 System Implementation

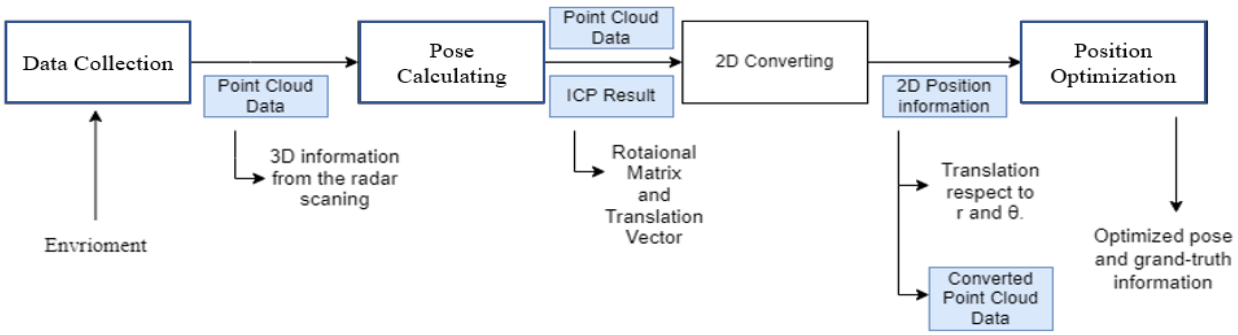

Figure 7.1: System Overview

The SLAM system designed in this thesis is implemented following a sequence of stages as shown in Figure 7.1, it contains four major stages, which are Data Collection, Pose Calculating, 2D Conversion, and Position optimization. In general, the first stage collects the IWR 1443 mmWave radar input with the format discussed in Chapter 5.2 and outputs a set of point cloud data that captures the radar measurement of the surrounding environment. The point cloud data from the first stage was shown in Figure 5.12, it includes the 3D information that is used by the ICP algorithm for the pose calculation. Those point clouds will be sorted based on the sequence of frames in chronological order, then the rotation and translation between each frame will be calculated in the second stage with the process described in Equation 5.1-5.3. Theoretically, the outputs of the second stage (i.e. the ICP algorithm) are the displacement and orientation information between the frames sampled from two adjacent positions. This information can be used to trace the moving trajectory. Following the target scenario, this research aims to generate a 2-D map with trajectory trace. Therefore, in order to minimize the negative effect caused by the translation and rotation along the z-axis, the third stage is to convert the ICP results into a 2D format. Lastly, the final stage will use the converted 2D positioning information for a further optimization to produce the SLAM output (i.e. a 2D map with movement trajectories). In this research, the iSAM2 algorithm is used to perform the optimization [80]. The details of each stage will be explained in the following subsections of this Chapter.

7.1 Data Collection

The sensed points that belong to the same detected frame are sent to the host following the packet structure and header information such as the number of frames, number of detected obstacles, and the number of TLVs as mentioned in Chapter 5.2. Among the header information, the number of TLV will

be used to sort the income data. In addition, the obtained information is not only affected by where and how the data is sampled, but also could be impacted by the parameter setting of the IWR1443. For instance, the CFAR value could affect the number of detected obstacles. The experiments that been conducted under the same physical environment and identical parameter setting showing different average numbers of detected obstacles per frame of 32.25 and 59.44 for the trials with CFAR value of 20 dB and 15 dB respectively. Therefore, to identify and minimize the negative effect caused by radar settings, various experiments have been conducted to evaluate the system performance under different radar settings. As the outcome, the following parameters are used in the following chapters if the parameter values are not specifically mentioned.

- Frequency Band: 77-81 GHz
- Frame Rate: 15 fps
- Range Resolution: 0.04 m
- Maximum Unambiguous Range: 8.19 m
- Maximum Radial Velocity: 2.67 m/s
- Radial Velocity Resolution: 0.34 m/s
- Range Detection Threshold (CFAR): 10 dB
- Range Peak Grouping: Disable
- Doppler Peak Grouping: Disable
- Static Clutter Removal: Disable

In practice, the ICP algorithm requires a large amount of point data (a dense point cloud), and hence every six consecutive frames will be merged into one. Moreover, the radar device is mounted on a user at a height that is 1.5 meters above the ground, and the antenna is always facing the marching direction. At the end of this stage, the point cloud data which contains the x, y, and z information of the detected obstacle and the number of frames that the point belongs is sent to the ICP processing stage.

7.2 Pose Calculation

The pose between two successive frames will be calculated by the ICP algorithm as mentioned in Chapter 6, and the walking path could be traced based on that information. In this thesis, the trajectory (the walking path) of the device is calculated as:

$$\begin{gathered} D = D + TT \\ TT = RTSUM * TT \end{gathered} \tag{7.1}$$

where *D* is a vector that contains the x, y, and z value (initialized with [0,0,0]) of the current location, the *TT* is a 1x3 translation vector representing the movement in three dimensions. The RTSUM is a 3x3 matrix that accumulates the rotation matrix from the first frame to the current, which could be expressed as:

$$RTSUM = RT * RTSUM \tag{7.2}$$

where the RT is a 3x3 rotation matrix representing the rotation of the current successive frame, and the RTSUM is initialized with an identity matrix.

However, as expressed in Equation 7.2, the rotation between each frame is accumulated throughout the iterative process of ICP and will result in an orientation distortion.

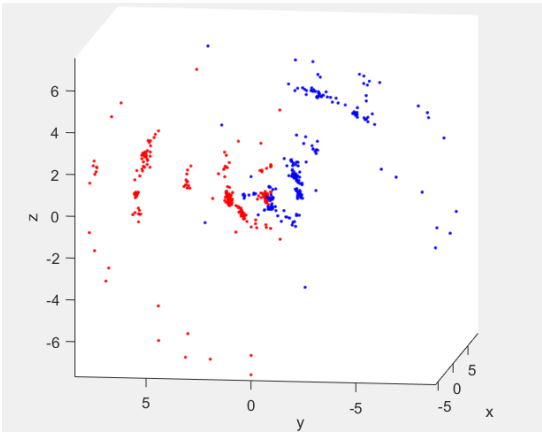

Figure 7.2: Point Twisting

Figure 7.2 shows the change in orientation, in which the red points are the original point cloud data, and the blue points are the rotated red points after applying the RTSUM on it. It is clearly showing that the features along the y-direction are changing to the z-direction after the rotation, which is not a valid situation as the radar should always facing forward. This kind of orientation twisting will cause the trajectory to go along the z-direction during the navigation, which is shown in the Figure 7.3.

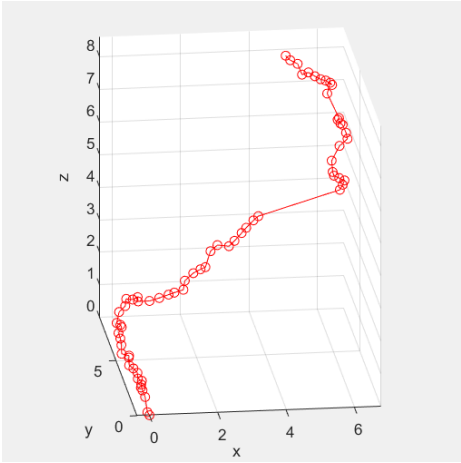

Figure 7.3: Example of Trajectory built by ICP Result

Figure 7.3 illustrates the situation which the trajectory is impacted by the orientation distortion, and clearly shows how the trajectory is deviated along the z-direction. Therefore, a 2D conversion process is performed after working out the displacement and trajectory to reduce the deviation along the z-direction.

7.3 2D Converting

Algorithm 1 Trajectory Rearranging

Input: R Rotation Matrix, T Translation Matrix, $Trajectory$ Trajectory matrix contains the location information

Output: $Trajectory$

```
for i < length(trajectory) do
    Calculate E, the euclidean distance between each continuous point ∈ Trajectory
    aveE ← E/length(trajectory)
    if E(i) > aveE × 1.2 then
        indicator = 1
    else if E(i) < aveE × 0.6 then
        indicator = 1
    else
        indicator = 0
    end if
    if indicator == 1 then
        R(i) ← R(i − 1)
        T(i) ← T(i − 1)
    end if
    Rebuild the Trajectory
end for

return Trajectory
```

Algorithm 7.1: Trajectory Rearranging

The process of converting the 3D results into a 2D space contains two steps, the first step is rearranging

the trajectory to correct the errors shown in Figure 7.3, followed by the second step of 2D projection of the corrected trajectory.

The trajectory is rearranged based on Algorithm 7.1. Firstly, the rotation matrix R, translation matrix T, and the trajectory matrix built in the previous stage (as Figure 7.3) will be read as input. The algorithm will loop over each point contained in the trajectory, and in each iteration, the Euclidian distance between every successive point will be calculated then work out an average distance.

Based on Chapter 7.1, the radar device is having a sample rate of 15 fps, in which a sample of the environment will be taken every 66.6 milliseconds. It is a considerably trivial time interval for the movement of human beings, especially in indoor conditions. Even after the frame merging, it still has an equivalent sampling rate at 2.5 fps, one sample per 0.4 seconds, which is also not a significant time interval for indoor activity. Thus, the points that represent the user's position should be approximately uniformly distributed on the walking path theoretically, in which the gap between each position should be relatively equal.

Based on this assumption, the trajectory could be evaluated by comparing the length between each point on it. In this thesis, for every successive point, if the distance between two successive points is larger than 1.2 times or less than 0.6 times of the average distance value, it will be rearranged. The rotation and translation matrix responsible for this displacement will be replaced with the ones from the previous points. After this step, the sorted trajectory is ready for the 2D projection. However, the process of trajectory rearranging only solve the deviation appears on the localization, but not orientation twisting, the error still exists when mapping the environment.
At this point, a sorted trajectory is available for the 2D projection. However, the process of trajectory rearranging only solve the deviation appears on the localization, but not orientation twisting, the error

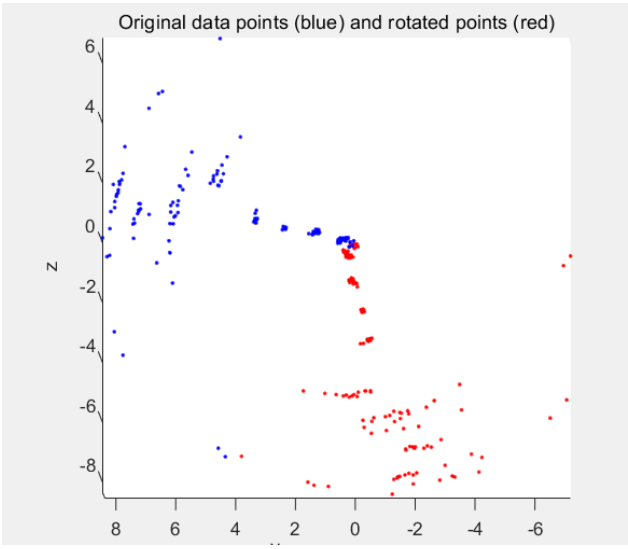

Figure 7.4: Example of Point Twisting (2)

still exists when mapping the environment.

Figure 7.4 shows the rotation of the sampled environmental features based on the Equation 7.2, using the rotation matrix updated by Algorithm 1, and Figure 7.4 is illustrating the same problem as Figure 7.2. As the solution, the whole trajectory will be projected onto a 2D plane and the displacement will be converted from rotation and translation matrix form to the θ, angle with respect to x-axis, and r, the Euclidian distance between each pair of consecutive points. The similar process is also applied to the sampled point cloud to re-calculate the angle and length between the aimed position and the corresponding measurement.

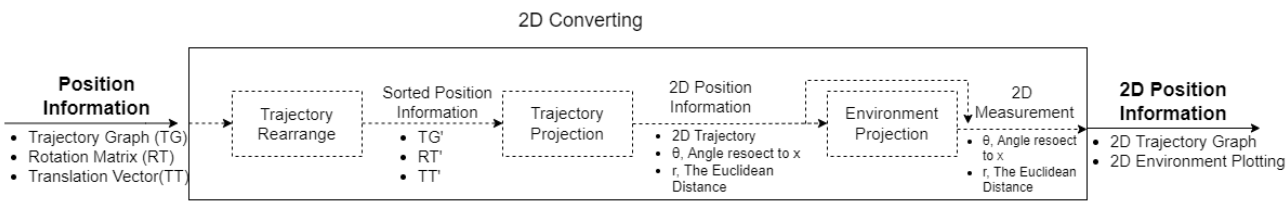

Figure 7.5: Flowchart for 2D Converting Stage

In conclusion, the details of the processing chain of the 2D conversion stage are summarized in Figure 7.5. The position information from the previous stage is used as the input, and the rearrangement will be performed in the first step to work out an updated positioning information. After that, the trajectory will be firstly projected onto a 2D plane with the angle and length information, and then the environment features (i.e. the landmarks or the obstacles in the physical environment) will also be projected. At the output, the projected localization and mapping information will be combined to build up the navigation map. The outcome of this stage will be further analyzed and discussed in Chapter 8.

7.4 Further Optimization

The last stage is the Further Optimization, which involves performing the iSAM2 algorithm (which has been introduced in Chapter 4.2.2) based on the 2D information produced in the previous stage. The iSAM2 algorithm is designed for incremental updates, which offers the capability to operate in real-time. Even though the experiment trials discussed in this thesis are done offline, in which the sampling of the environment is completed before the optimization stage, the incremental update features are still used by performing the iSAM2 algorithm iteratively.

In practice, the iSAM2 update can be separated into three steps, which are factor adding, setting an initial guess, and calculating the best estimation. The location and map information will be labeled as X and L respectively, in which the X is the location information that represents the points (pose), and the

L is the map information representing the landmarks, as discussed in Chapter 4.2.2. The factor adding step is for updating the factor graph which was illustrated in Chapter 4.2.2. In practice, the X and L will be treated as variables, and the constraints (factor) are 2D position information calculated in the 2D conversion stage. The position information will also be used as the initial guess at the same time, and the estimation calculation.

8 Experiments

In this Chapter, the SLAM algorithm with the mapping and trajectory tracing mentioned in the previous chapter will be demonstrated, evaluated and discussed in this Chapter. The parameters of the developed mmWave system will follow the same values presented in Chapter 7.1.

Three sets of experiments have been conducted to evaluate the performance of the system, all the experiment trials are completed using a square corridor with an inner wall of approximately 6.8 meters long, and 9 meters long for the outer wall of each side.

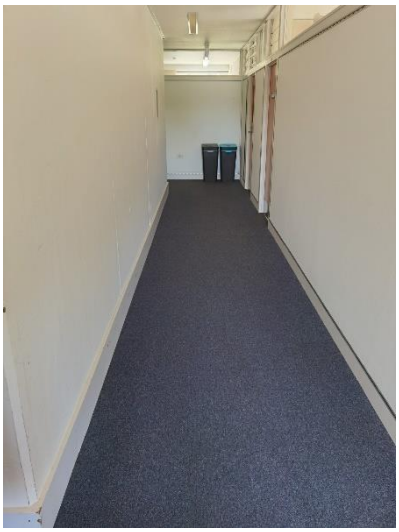

Figure 8.2: Viewing of The Corridor

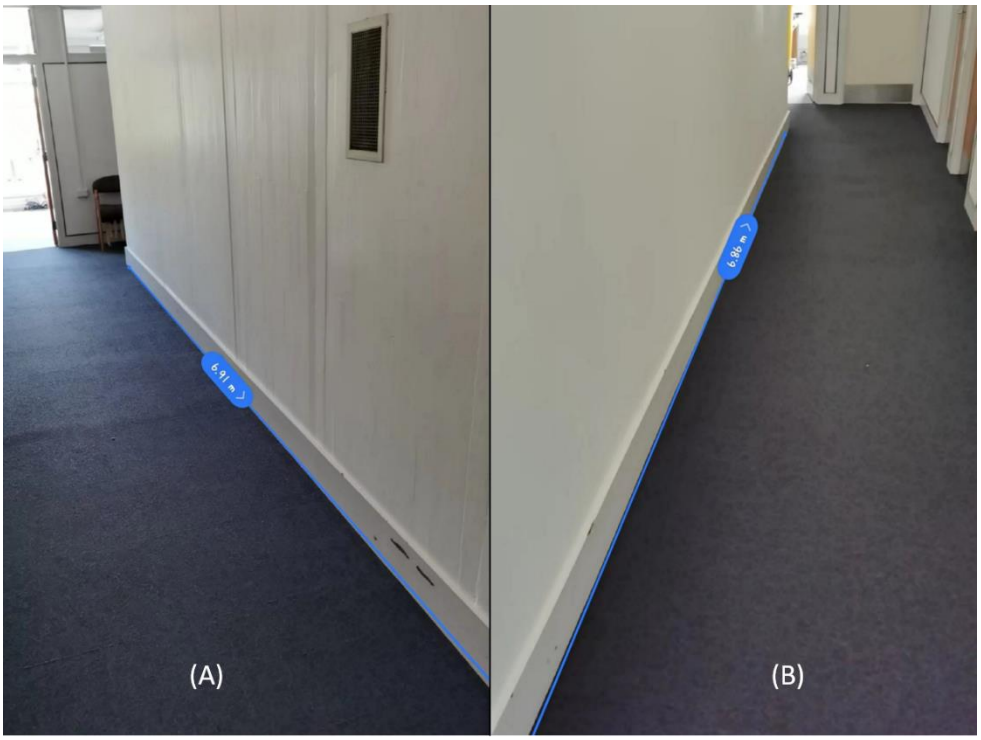

Figure 8.1: Viewing of Two Adjacent Corridor

One view of a segment of the square shape corridor is shown in Figure 8.1, and the corridor consists of four similar segments. The top view of the corridor is shown in Figure 8.2 below, where the black lines represent the inner and outer wall and the width of the corridor is approximately 2 meters. The blue line is the ground truth walking path in our trial experiment. The four segments (A), (B), (C), and (D) will be used together or separately in different experiments

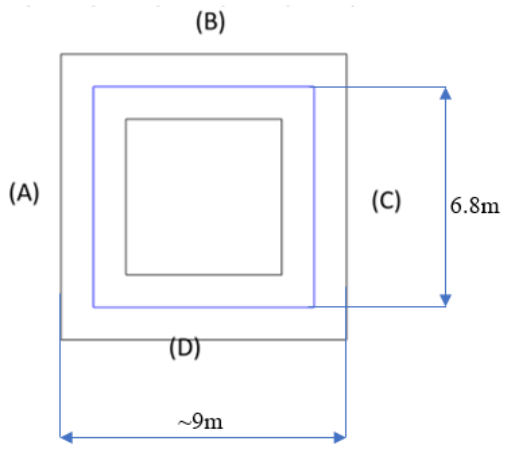

Figure 8.3:The Schematic of The Square Corridor

In this thesis, to evaluate the system performance under different experimental trials, the RMS value is used.

$$RMS = \sqrt{\frac{\sum_{i=1}^{n}(Z_i - X_i)^2}{N}} \tag{7.1}$$

Where the *N* is the number of sample data to be evaluated; Z is the ground truth value; X is the sample value to be evaluated. In a typical localization scenario, it is impossible to find the exact ground truth point that matches with the estimated location. Therefore, the linearly projected Z_i on the ground truth walking path is considered as the reference value.

8.1 Straight-Line Test

A straight-line test has been conducted at the segment (A) illustrated in Figure 8.3, where the user will start with the origin (0,0), and stop at the end of the inner wall nearly segment (B).

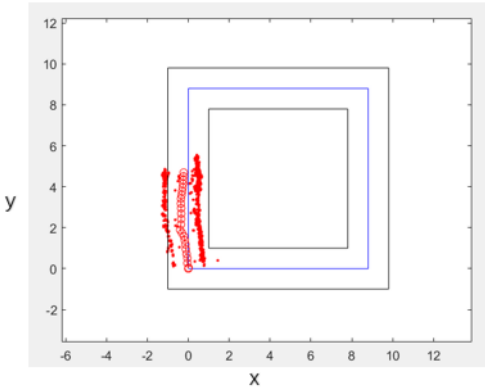

Figure 8.4: ICP Result for Straight-Line Test Trial 1

The solid dots in Figure 8.4 represent the environment features (or sometimes referred to as the landmarks), which are the walls in this case, and the hollow dots show the user's trajectory. Referring to Figure 8.4, a linear pathway is shown clearly in both the trajectory and the environment. More specifically, the RMS value of the estimated trajectory and the reference ground truth (i.e. the blue line) is 0.25 meters, and is 0.45 meters between the estimated environment features (i.e. the solid red dots) and the wall reference (i.e. the dark lines). This means under the straight walking path, the accuracy of the navigation map build purely by ICP result can achieve a submeter-level accuracy.
However, the total length of the path should be 6.8 meters, and the trajectory is shown on the graph

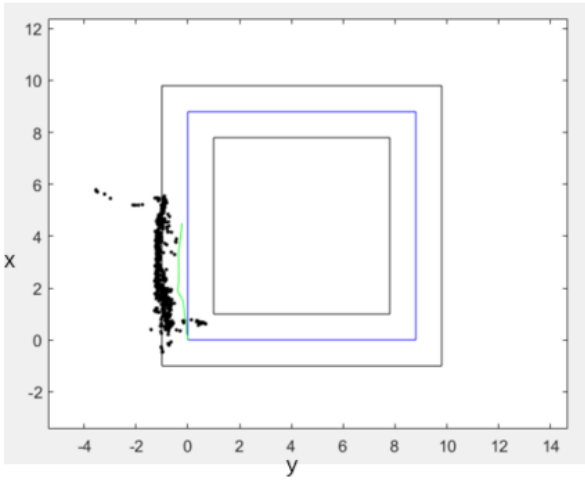

Figure 8.5: iSAM2 Result for Straight-Line Test Trial 1

only has 4.6 meters, which results in a 2.2 meters error.

As discussed in Chapter 7, the ICP result will be sent to the iSAM2 for further optimization. The result is shown in Figure 8.5, in which the green line represents the optimized trajectory, and the dark solid point is the environmental features. The same criteria are used to evaluate the iSAM2 results, giving a RMS value of 0.26 meters in the estimated walking trajectory, a RMS value of 0.29 meters in the estimated landmark locations, and a total travelled distance of 4.6 meters. In this case, the iSAM2 algorithm is able to achieve a slight improvement in the landmark estimation.

While the iSAM2 seems to offer a better result as the RMS value is slightly smaller than the ICP result, the graphical results show in Figure 8.5 shows that some points representing the inner wall have been trimmed out during the optimization process.

The same experiment has been conducted 3 times to ensure the results are reliable and replicable. The results of the three experiments are summarized in Table 8.1. Baes on the table, it is obvious that both ICP and iSAM2 results are offering a trajectory and landmarks with a position that is very close to the reference ground truth, and the iSAM2 result is slightly better. However, loss of information may happen during the optimization process in iSAM2.

	ICP	ICP	ICP	iSAM2	iSAM2	iSAM2
	1	2	3	1	2	3
Location RMS value (m)	0.25	0.38	0.25	0.26	0.16	0.18
Mapping RMS value (m)	0.45	0.62	0.48	0.29	0.35	0.34
Distance Difference (m)	2.2	1.5	0.88	2.2	1.8	0.86

Table 8.1: Straight-Line Test Result

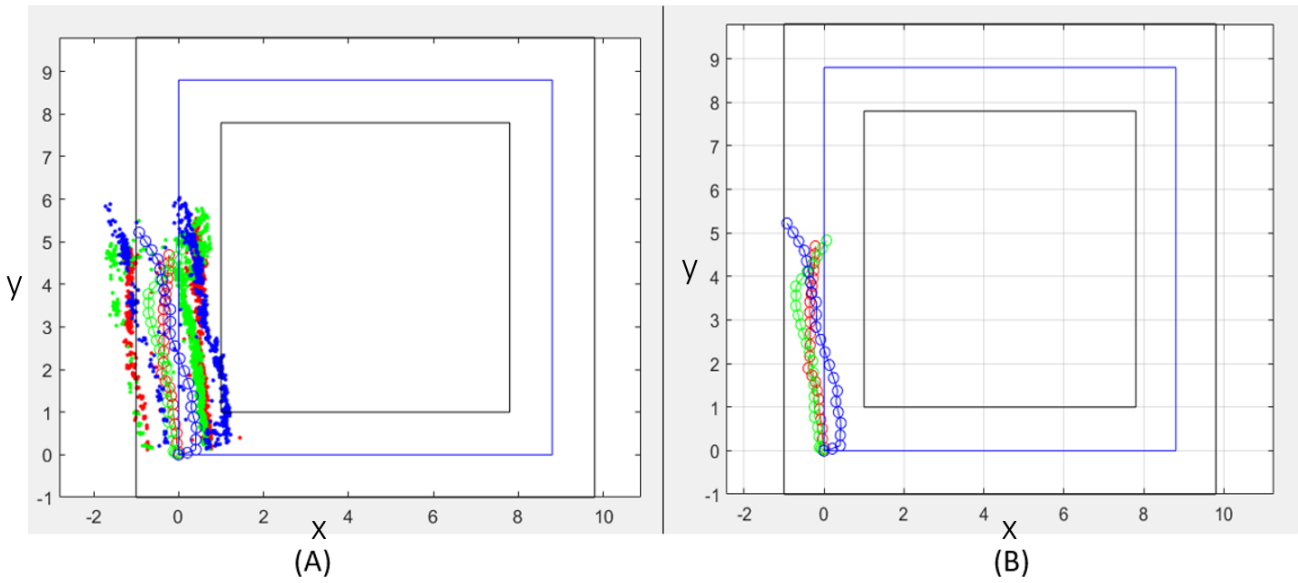

Figure 8.6: The Graphical Result for All Trials in Straight-Line Test (ICP)

In addition, it is important to ensure the result achieved by the system is stable, which means no significant variations across different trials. Figure 8.6 plots the three ICP results in Table 8.1 in one figure, the Figure 8.6 (a) contains both the trajectory and environment features and Figure 8.6 (b) only shows the trajectory. Those three experiments' result is colored red, green, and blue respectively. Referring to the figure, the three paths largely overlap with each other with the blue path slightly deviates from the reference path, which show a relatively stable result.

To evaluate the stability of the experiment result, the RMS value is calculated using the difference between each pair of paths, which shown in the table below.

	Red-green	Red-Blue	Green-Blue	Average
Trajectory (m)	0.2	0.39	0.49	0.36
Landmark (m)	0.12	0.26	0.31	0.23

Table 8.2: ICP RMS Difference Result (Straight-Line Test)

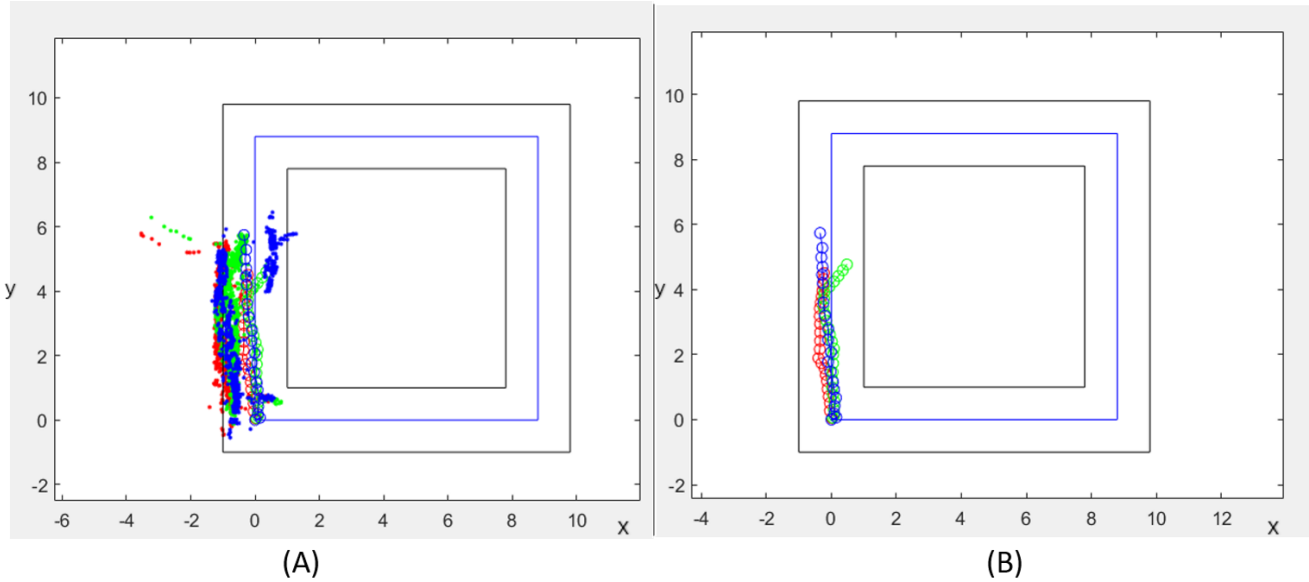

Figure 8.7: The Graphical Result for All Trials in Straight-Line Test (ISAM2)

The similar step is also applied to the iSAM2 result, as shown in Figure 8.7. The optimized iSAM2 result is more closely following the reference path than the ICP result. The RMS values of the difference between each pair of experiments are listed in following table.

	Red-green	Red-Blue	Green-Blue	Average
Trajectory (m)	0.3	0.38	0.43	0.37
Landmark (m)	0.17	0.59	0.34	0.37

Table 8.3: iSAM2 RMS Difference Result (Straight-Line Test)

As shown in Table 8.3, the trajectory from the iSAM2 result is more stable than the ICP one, as the differences between each pair of trials in the iSAM2 is less than the differences in the ICP results. The iSAM2 algorithm also achieved an insignificant average difference between each trial.

Overall, in the straight-line test, the iSAM2 has achieved a slightly better performance than the ICP, but it will cause some data loss during the optimization process. To further evaluate and compare the performance of the ICP and iSAM2 algorithm, the L-shape and U-shape path are tested in the next two subsections.

8.2 L-Shape Test

Different from the straight-line test, the L shape test also involves a 90-degree turn (change in orientation) which makes the localization and mapping more challenging. The walking path of the user is approximately 13.6 meters, including both segment (A) and (B). The user starts from the bottom-left corner, and stop at the top-right corner .

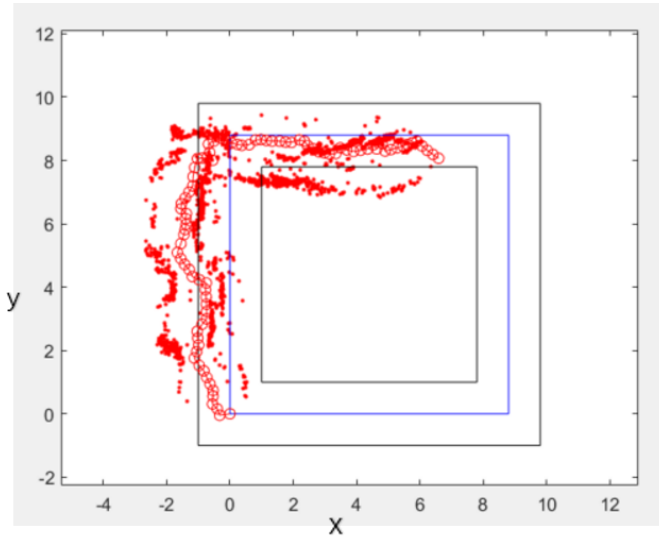

Figure 8.8: ICP Result for L Shape Test Trial 1

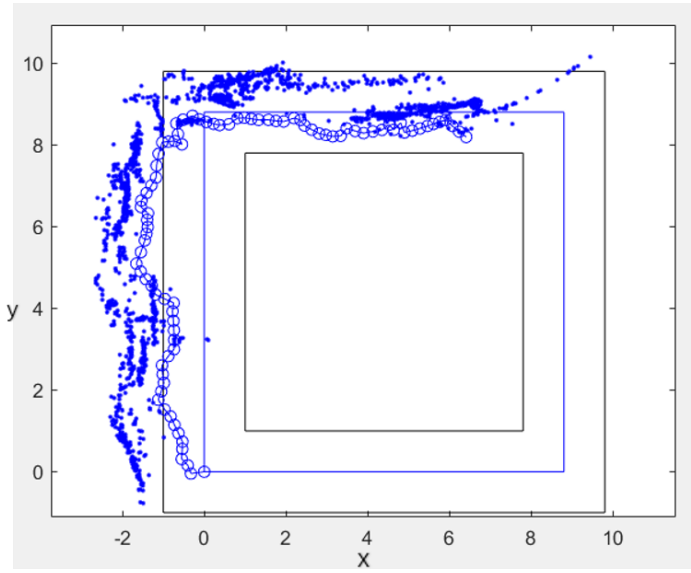

Figure 8.9: ISAM2 Result for L Shape Test Trial 1

Referring to Figure 8.8, both the trajectory and the environmental features are clearly reflecting an L-shape pathway, with the turning motion. In Figure 8.9, a similar observation can also be obtained in the iSAM2 result, and the loss of information that occurred in the straight-line test still exists. However, the distribution of the points that represent the environmental features in Figure 8.9 is more

concentrated to give a clearer indication of the landmarks (i.e. the walls), and the features are less overlapped with the trajectory after optimization, in comparison with the results in Figure 8.8.

	ICP	ICP	ICP	iSAM2	iSAM2	iSAM2
	1	2	3	1	2	3
Location RMS value (m)	0.81	0.74	0.60	0.81	0.69	0.6
Mapping RMS value (m)	0.66	0.56	0.59	0.81	0.58	0.66
Distance (m)	1.1	1.5	1	1	1.7	0.9

Table 8.4: L-Shape Test Result

Table 8.4 is showing the criteria used to evaluate the ICP and iSAM2 results for L-shape testing. The RMS differences of the L-shape test experience a significant increase compared with the straight-line test result, which is inside of expectation as the total distance and the spatial complexity (the change in orientation is involved) of the path is increased. The iSAM2 is still showing slightly better performance at the trajectory building as the iSAM2 result it tends to have a less RMS value in location difference.

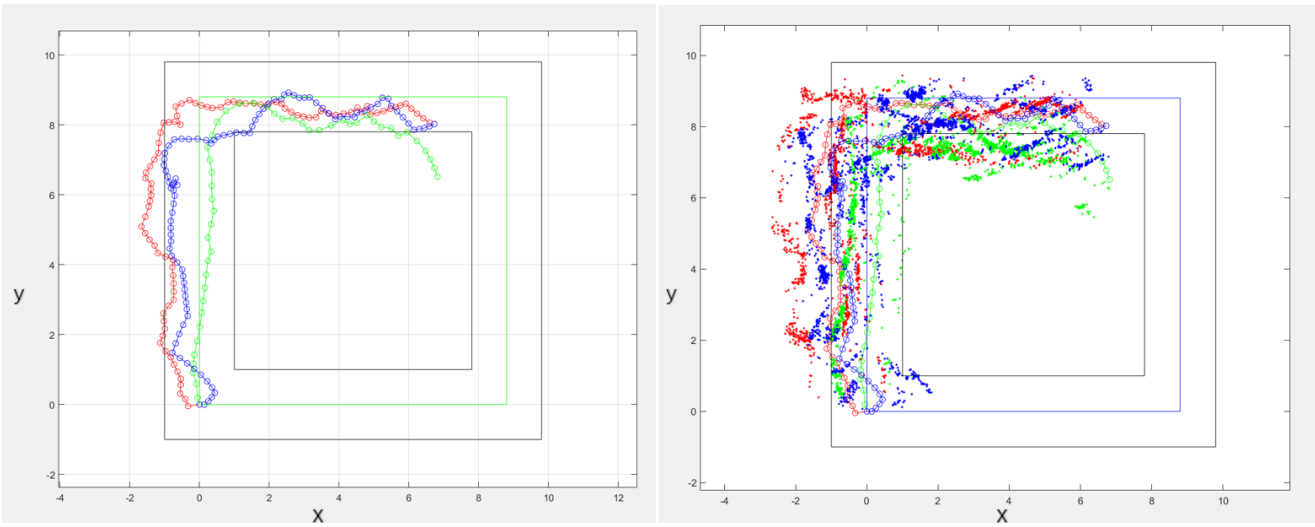

(A) (B)

Figure 8.10: The Graphical Result for All Trials in L-Shape Test (ICP)

	Red-green	Red-Blue	Green-Blue	Average
Trajectory (m)	0.86	0.47	0.7	0.68
Landmark (m)	0.34	0.33	0.46	0.38

Table 8.5: ICP RMS Difference Result (L-Shape Test)

Referring to Figure 8.10 (A), it can be tall that all ICP result is showing an L shape feature, and the red and blue trial seems to have a more similar shape than the green trial.

Table 8.5 shows the difference of the trajectory and landmark points between two of the ICP results. As mentioned earlier, the trajectory difference between the red and blue trials is less in comparison with the green trial. Moreover, compare with the value listed in Table 8.2, the error among different experiment trials is increasing. However, the result still could be evaluated as relatively stable, as the average RMS value shown in Table 8.5 achieved a submeter accuracy, which indicates the results are accurate and repeatable

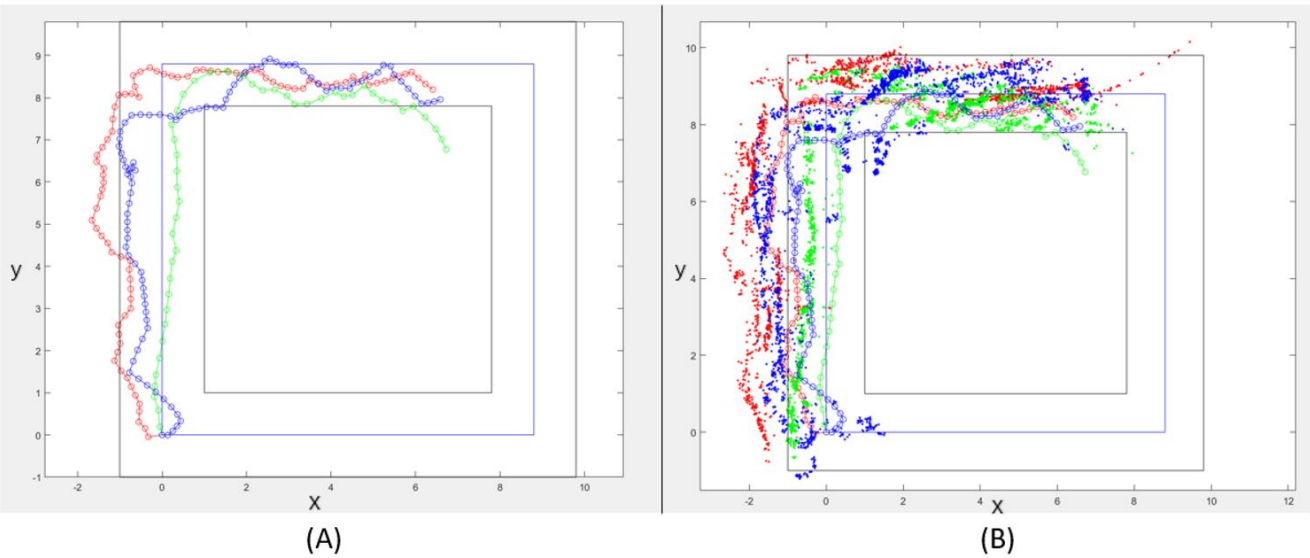

Figure 8.11: The Graphical Result for All Trials in L-Shape Test (ISAM2)

	Red-green	Red-Blue	Green-Blue	Average
Trajectory (m)	0.85	0.48	0.71	0.68
Landmark (m)	0.47	0.67	0.68	0.61

Table 8.6: ISAM2 RMS Difference Result (L-Shape Test)

Figure 8.11 is showing the three repeated experiment results of the iSAM2 algorithm as the navigation map. The difference between the trajectories of two trials achieved by the iSAM2 algorithm is almost as same as the values listed in Table 8.5 for the ICP algorithm. However, Table 8.6 shows a significant increase in the RMS value for the landmark points with an average value of 0.61 meter (vs. 0.38 meter for the ICP). This could be explained as the ICP results contain both the inner and the outer wall, whereas the iSAM2 results contain mostly just the outer wall. This could lead to the issue that some points representing the inner wall in a trial actually compared to the points for the outer wall in the other trials, which can lead to a misconducted RMS value.

However, its sill offers a sub-meter level accuracy as both the difference among trials or between the trials and reference is less than one meter, which means the iSAM2 has a reasonable accuracy and stability.

Based on the L-shape test results, it can be told that both the ICP and iSAM2 results are showing reasonable performance with submeter accuracy and both algorithms are able to handle the movements with changing orientation (i.e. turning). The observed results are consistent with the straight-line test and further verified the validity and performance of the proposed algorithms

8.3 U-Shape Test

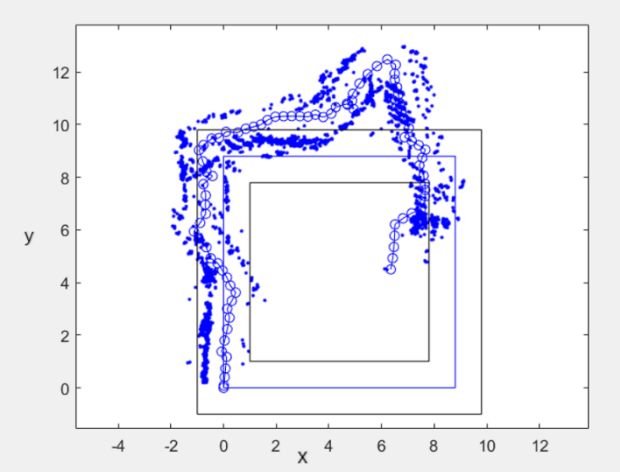

Figure 8.12: ICP Result for U-Shape Test Trial 1

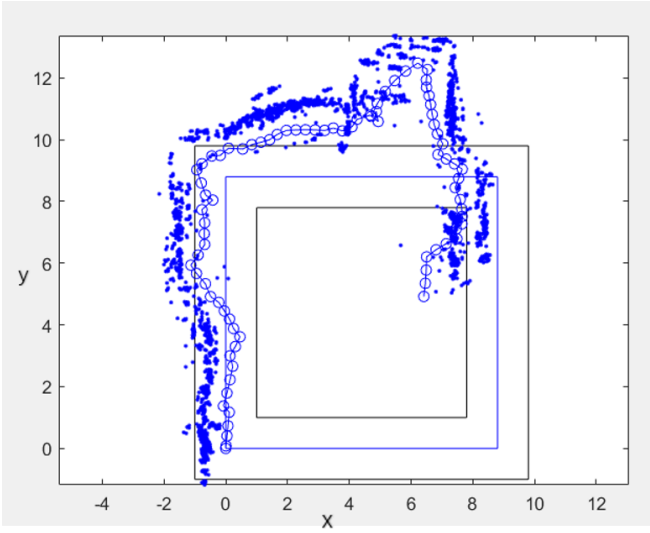

Figure 8.13: ISAM2 Result for U-Shape Test Trial 1

The U-shape test is a further extension to evaluate the system performance under more complex movement and spatial variations. The user is starting from the bottom-left corner and stopping at the bottom-right corner, which involves three segments (A, B and C) of the corridor and two 90 degree turns. The total walking distance is about 20.4 meters. From the graph, a strong U-shape feature could be detected, based on this, it is reasonable to argue that this graph is reflecting the real-world situation.

Referring to Figure 8.13, a clear U-shape navigation map is produced by the ICP algorithm which reflects the actual motion of the experiment.

	ICP	ICP	ICP	iSAM2	iSAM2	iSAM2
	1	2	3	1	2	3
Location RMS difference (m)	1.5	0.94	1.16	1.5	0.94	1.15
Mapping RMS Difference (m)	0.89	0.67	0.74	1.19	0.73	0.67
Distance (m)	8.7	1.13	4.6	8.31	0.97	4.26

Table 8.7: U-Shape Test Result

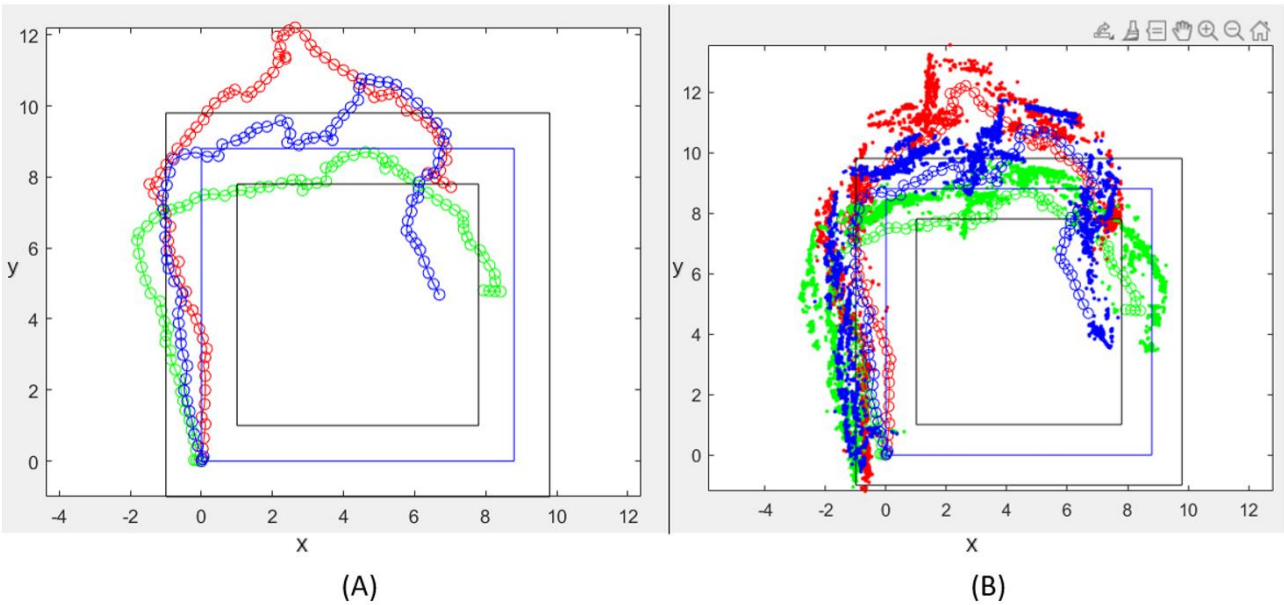

Figure 8.14: The Graphical Result for All Trials in U-Shape Test (iSAM2)

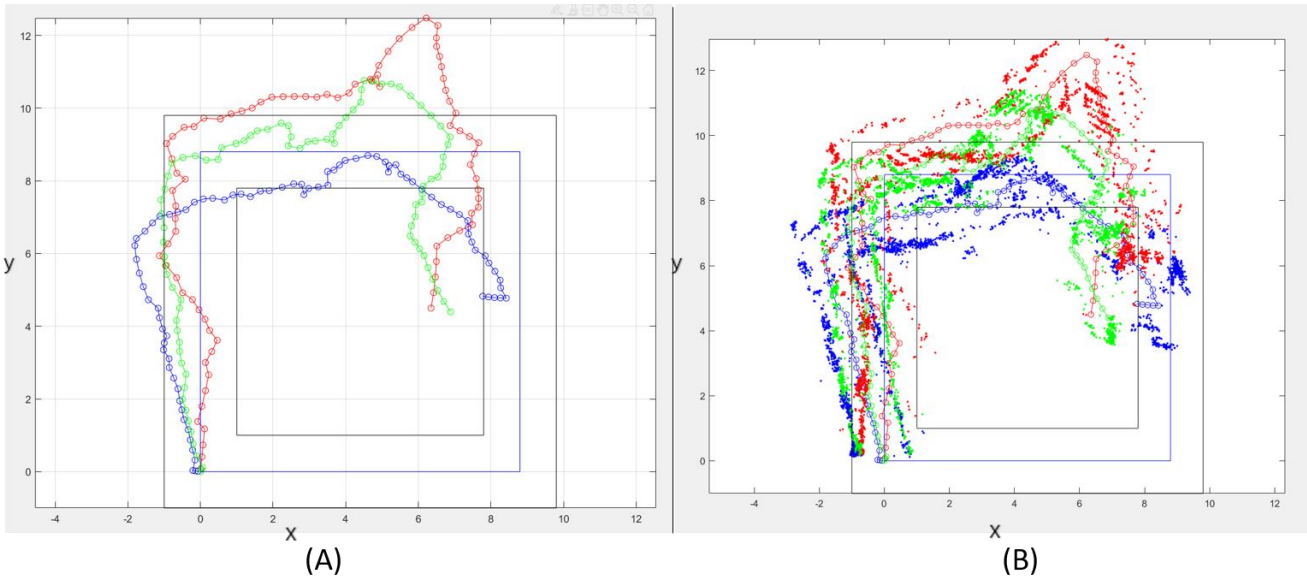

Figure 8.15: The Graphical Result for All Trials in U-Shape Test (ICP)

The U-shape navigation map and trajectory is also generated after the optimization process of the iSAM2 algorithm. Based on the visual inspection of Figure 8.14 and 8.15, it can also be found that there is less data overlap between the trajectory and environment features in the iSAM2 result. However, most inner wall data points are filtered out by the iSAM2 optimization process.

From the data listed in Table 8.8, it is clear that the RMS value between the system generated path and the reference path are increasing more significantly in comparison with the straight-line and L-shape path. This increase in RMS value is primarily caused by the longer distance traced and with more complex motions involved (i.e. more frequent change of orientation).

	Red-green	Red-Blue	Green-Blue	Average
Trajectory (m)	1.6	1.0	1.1	1.2
Landmark (m)	1.0	0.8	0.7	0.89

Table 8.8: ICP RMS Difference Result (U-Shape Test)

	Red-green	Red-Blue	Green-Blue	Average
Trajectory (m)	1.6	1.0	1.1	1.2
Landmark (m)	1.0	0.76	0.8	0.89

Table 8.9: ISAM2 RMS Difference Result (U-Shape Test)

From the Table 8.8 and 8.9, the difference between each pair of experiment trials is also increasing, which is again contributed by the longer travel distance and higher spatial complexity. With more turns, the error caused by the orientation distortion mentioned in Chapter 7 is more frequent and severe, and hence leads to the request of replacing the moving constraints (the rotation and translation) between the points increase.

While the results of the U-shape path not achieved submeter accuracy, the results do demonstrate the correct overall motion and relative environment features along the pathway. This statement is consistent across all three experiments (i.e. straight-line, L-shape path, and U-shape path), which gives a good indication of the validity and performance of the proposed algorithm. However, the errors do accumulate and grow with distance and increasing motion complexity. The iSAM2 optimization also not offering a significant improvement compare to the ICP result. Further research will need to be conducted in the future to investigate these issues.

9 Conclusion and Future Work

In modern society, location information has proved its value in many real-world applications, such as outdoor navigation, logistic control, and goods tracking. While GPS technology dominates the outdoor applications, indoor positioning and navigation technologies still facing many challenges without stable presence of GPS and cellular network signals. Very often, existing indoor positioning technologies require pre-installed infrastructures or pre-determined knowledge about the environment, which largely limit the practicality of these technologies. In this thesis, a self-contained indoor localization and mapping technique is developed using the state-of-the-art mmWave technology. The developed system aims to enable mapping of the surrounding environment, and localizing and tracing the movement trajectory without any prior knowledge of the environment or pre-installed infrastructures.

In this thesis, a graph-based indoor SLAM option is proposed based on the combination of the ICP and iSAM2 algorithm to process the point cloud data collected by only one IWR1443 mmWave radar device. The purpose of the ICP algorithm is to map and trace the moving object by comparing each consecutive pair of point cloud frames. The ICP algorithm allows the system to solve SLAM problem without involving an IMU device, which is the most commonly used approach for providing orientation information. The iSAM2 algorithm is adopted to provide further optimization to smooth the navigation map and trajectory trace. The developed system is evaluated with three experiments with different walking paths (i.e. straight line, L shape, and U shape) in a square shape corridor. The experiment results show that the proposed system can achieve submeter accuracy in simple paths such as straight-line or L-shape movements. However, with higher spatial complexity (i.e. frequently change in orientation), the accuracy will decrease over time. Even though there is a data loss that happens during iSAM2 caused by its graph update algorithm, it is still reasonable to state that the system is offering the capability to complete the indoor SLAM with only one sensor, and the ICP combined with iSAM2 design do achieve slight improvement in accuracy than a sole ICP system.

Several research directions are planned to further investigate the proposed technique and to enhance the system performance in a more complex environment such as shopping mall, University campuses, or large business building.

First, the long-term performance requires further investigation. How to reduce error accumulation and allow long-term localization with submeter accuracy is a key challenge that needs to be addressed. Second, it is important to address the challenge of extending the mapping and positioning scenario to support a 3D environment.

Last but not least, it is important to investigate the real-time performance of the proposed technique to maximize the potential of the iSAM2 algorithm (e.g., with a better trajectory re-arrangement option) to further improve the accuracy

References

[1] Lee G and Yim J, "A Review of the Techniques for Indoor Location based Service," Mar. 2012. Accessed: Jan. 26, 2022. [Online]. Available: https://citeseerx-ist-psu-edu.ezproxy.auckland.ac.nz/viewdoc/download?doi=10.1.1.386.6813&rep=rep1&type=pdf

[2] M. Youssef, "Indoor Localization," *Encyclopedia of GIS*, pp. 547–552, 2008, doi: 10.1007/978-0-387-35973-1_622.

[3] S. Jochen and V. Agnès, "Location-Based Services 1st Edition," p. 255, 2004, Accessed: Jan. 27, 2022. [Online]. Available: https://www.elsevier.com/books/location-based-services/schiller/978-1-55860-929-7

[4] A. Damani, H. Shah, K. Shah, M. Vala, and A. Professor, "Global Positioning System for Object Tracking," *International Journal of Computer Applications*, vol. 109, no. 8, pp. 975–8887, 2015.

[5] H. Du, C. Zhang, Q. Ye, W. Xu, P. L. Kibenge, and K. Yao, "A hybrid outdoor localization scheme with high-position accuracy and low-power consumption," *Eurasip Journal on Wireless Communications and Networking*, vol. 2018, no. 1, pp. 1–13, Dec. 2018, doi: 10.1186/S13638-017-1010-4/FIGURES/12.

[6] C. Drane, M. Macnaughtan, and C. Scott, "Positioning GSM telephones," *IEEE Communications Magazine*, vol. 36, no. 4, pp. 46–59, 1998, doi: 10.1109/35.667413.

[7] M. Ibrahim and M. Youssef, "CellSense: A probabilistic RSSI-based GSM positioning system," *GLOBECOM - IEEE Global Telecommunications Conference*, 2010, doi: 10.1109/GLOCOM.2010.5683779.

[8] Q. Liu, H. Lu, H. Zhang, and B. Zou, "Research and design of intelligent vehicle monitoring system based on GPS/GSM," *ITST 2006 - 2006 6th International Conference on ITS Telecommunications, Proceedings*, pp. 1267–1270, 2006, doi: 10.1109/ITST.2006.288858.

[9] M. A. Al-Khedher, "Hybrid GPS-GSM Localization of Automobile Tracking System," *International Journal of Computer Science & Information Technology (IJCSIT)*, vol. 3, no. 6, 2011, doi: 10.5121/ijcsit.2011.3606.

[10] B. P. S. Sahoo and S. Rath, "Integrating GPS, GSM and Cellular Phone for Location Tracking and Monitoring".

[11] H. Wang *et al.*, "Mobile Robot Indoor Positioning System Based on K-ELM," *Journal of Sensors*, vol. 2019, 2019, doi: 10.1155/2019/7547648.

[12] F. de Cillis, F. de Simio, L. Faramondi, F. Inderst, F. Pascucci, and R. Setola, "Indoor positioning system using walking pattern classification," *2014 22nd Mediterranean Conference on Control and Automation, MED 2014*, pp. 511–516, Nov. 2014, doi: 10.1109/MED.2014.6961424.

[13] N. E. Tabbakha, W. H. Tan, and C. P. Ooi, "Indoor location and motion tracking system for elderly assisted living home," *Proceeding of 2017 International Conference on Robotics, Automation and*

Sciences, ICORAS 2017, vol. 2018-March, pp. 1–4, Mar. 2018, doi: 10.1109/ICORAS.2017.8308073.

[14] F. Santoso and S. J. Redmond, "Indoor location-aware medical systems for smart homecare and telehealth monitoring: state-of-the-art," *Physiological Measurement*, vol. 36, no. 10, p. R53, Aug. 2015, doi: 10.1088/0967-3334/36/10/R53.

[15] M. Maheepala, A. Z. Kouzani, and M. A. Joordens, "Light-Based Indoor Positioning Systems: A Review," *IEEE Sensors Journal*, vol. 20, no. 8, pp. 3971–3995, Apr. 2020, doi: 10.1109/JSEN.2020.2964380.

[16] S. Xia, Y. Liu, G. Yuan, M. Zhu, and Z. Wang, "Indoor Fingerprint Positioning Based on Wi-Fi: An Overview," *ISPRS International Journal of Geo-Information*, vol. 6, no. 5, p. 135, Apr. 2017, doi: 10.3390/ijgi6050135.

[17] A. Waqar, I. Ahmad, D. Habibi, and Q. V. Phung, "Analysis of GPS and UWB positioning system for athlete tracking," *Measurement: Sensors*, vol. 14, p. 100036, Apr. 2021, doi: 10.1016/J.MEASEN.2020.100036.

[18] H. Liu, H. Darabi, P. Banerjee, and J. Liu, "Survey of wireless indoor positioning techniques and systems," *IEEE Transactions on Systems, Man and Cybernetics Part C: Applications and Reviews*, vol. 37, no. 6, pp. 1067–1080, Nov. 2007, doi: 10.1109/TSMCC.2007.905750.

[19] M. A. Al-Ammar *et al.*, "Comparative survey of indoor positioning technologies, techniques, and algorithms," *Proceedings - 2014 International Conference on Cyberworlds, CW 2014*, pp. 245–252, Dec. 2014, doi: 10.1109/CW.2014.41.

[20] J. Mier, A. Jaramillo-Alcázar, and J. J. Freire, "At a Glance: Indoor Positioning Systems Technologies and Their Applications Areas," *Advances in Intelligent Systems and Computing*, vol. 918, pp. 483–493, Feb. 2019, doi: 10.1007/978-3-030-11890-7_47.

[21] T. H. Dinh, T. Pham, and P. Doan Tinh, "Fingerprinting-based Indoor Positioning with Variable Power Maps," 2018, Accessed: Jan. 29, 2022. [Online]. Available: https://www.researchgate.net/publication/327602408

[22] A. Varshavsky, E. de Lara, J. Hightower, A. Lamarca, and V. Otsason, "GSM indoor localization," *Pervasive and Mobile Computing*, vol. 3, pp. 698–720, 2007, doi: 10.1016/j.pmcj.2007.07.004.

[23] A. Azeez *et al.*, "Wireless Indoor Localization Systems and Techniques: Survey and Comparative Study Comparative Study," *Indonesian Journal of Electrical Engineering and Computer Science*, vol. 3, no. 2, pp. 392–409, 2016, doi: 10.11591/ijeecs.v3.i2.pp392-409.

[24] F. Liu *et al.*, "Survey on WiFi-based indoor positioning techniques," *IET Communications*, vol. 14, no. 9, pp. 1372–1383, Jun. 2020, doi: 10.1049/IET-COM.2019.1059/CITE/REFWORKS.

[25] C. Yang and H. R. Shao, "WiFi-based indoor positioning," *IEEE Communications Magazine*, vol. 53, no. 3, pp. 150–157, Mar. 2015, doi: 10.1109/MCOM.2015.7060497.

[26] S. Xia *et al.*, "Indoor Fingerprint Positioning Based on Wi-Fi: An Overview," *ISPRS International Journal of Geo-Information 2017, Vol. 6, Page 135*, vol. 6, no. 5, p. 135, Apr. 2017, doi: 10.3390/IJGI6050135.

[27] J. Kim and D. Han, "Passive WiFi Fingerprinting Method," *IPIN 2018 - 9th International Conference on Indoor Positioning and Indoor Navigation*, Nov. 2018, doi: 10.1109/IPIN.2018.8533788.

[28] A. Satan and Z. Toth, "Development of bluetooth based indoor positioning application," *2018 IEEE International Conference on Future IoT Technologies, Future IoT 2018*, vol. 2018-January, pp. 1–6, Mar. 2018, doi: 10.1109/FIOT.2018.8325586.

[29] A. Satan, "Bluetooth-based indoor navigation mobile system," *Proceedings of the 2018 19th International Carpathian Control Conference, ICCC 2018*, pp. 332–337, Jun. 2018, doi: 10.1109/CARPATHIANCC.2018.8399651.

[30] K. C. Lai, B. H. Ku, and C. Y. Wen, "Using cooperative PIR sensing for human indoor localization," *2018 27th Wireless and Optical Communication Conference, WOCC 2018*, pp. 1–5, Jun. 2018, doi: 10.1109/WOCC.2018.8372703.

[31] D. Yang, B. Xu, K. Rao, and W. Sheng, "Passive Infrared (PIR)-Based Indoor Position Tracking for Smart Homes Using Accessibility Maps and A-Star Algorithm," *Sensors 2018, Vol. 18, Page 332*, vol. 18, no. 2, p. 332, Jan. 2018, doi: 10.3390/S18020332.

[32] F. von Zabiensky, M. Kreutzer, and D. Bienhaus, "Ultrasonic Waves to Support Human Echolocation," *Lecture Notes in Computer Science (including subseries Lecture Notes in Artificial Intelligence and Lecture Notes in Bioinformatics)*, vol. 10907 LNCS, pp. 433–449, Jul. 2018, doi: 10.1007/978-3-319-92049-8_31.

[33] F. Hoeflinger, A. Saphala, D. J. Schott, L. M. Reindl, and C. Schindelhauer, "Passive Indoor-Localization using Echoes of Ultrasound Signals," *2019 International Conference on Advanced Information Technologies, ICAIT 2019*, pp. 60–65, Nov. 2019, doi: 10.1109/AITC.2019.8921282.

[34] M. Jin, B. Koo, S. Lee, C. Park, M. J. Lee, and S. Kim, "IMU-assisted nearest neighbor selection for real-time WiFi fingerprinting positioning," *IPIN 2014 - 2014 International Conference on Indoor Positioning and Indoor Navigation*, pp. 745–748, 2014, doi: 10.1109/IPIN.2014.7275556.

[35] "Enhanced WiFi ToF Indoor Positioning System with MEMS Based INS and Pedometric Information." https://www.ion.org/publications/abstract.cfm?articleID=11613 (accessed Apr. 26, 2022).

[36] R. Salman and I. Willms, "A mobile security robot equipped with UWB-radar for super-resolution indoor positioning and localisation applications," *2012 International Conference on Indoor Positioning and Indoor Navigation, IPIN 2012 - Conference Proceedings*, 2012, doi: 10.1109/IPIN.2012.6418927.

[37] "Knowledge-based Indoor Positioning Based on LiDAR Aided Multiple Sensors System for UGVs." https://www.ion.org/publications/abstract.cfm?articleID=11637 (accessed Apr. 26, 2022).

[38] A. R. Khairuddin, M. S. Talib, and H. Haron, "Review on simultaneous localization and mapping (SLAM)," in *Proceedings - 5th IEEE International Conference on Control System, Computing and Engineering, ICCSCE 2015*, May 2016, pp. 85–90. doi: 10.1109/ICCSCE.2015.7482163.

[39] N. Azril, B. Zaman, S. Abdul-Rahman, S. Mutalib, and R. Shamsuddin, "Applying Graph-based SLAM Algorithm in a Simulated Environment", doi: 10.1088/1757-899X/769/1/012035.

[40] LEONARD and J., "Mobile robot lacalization by tracking geometric beacons," *IEEE Trans. Robot.*

Autom., vol. 7, no. 3, pp. 89–97, 1991, Accessed: Jan. 29, 2022. [Online]. Available: https://ci.nii.ac.jp/naid/10026185126

[41] S. Wang, Z. Wu, and W. Zhang, "An Overview of SLAM," *Lecture Notes in Electrical Engineering*, vol. 528, pp. 673–681, 2019, doi: 10.1007/978-981-13-2288-4_64.

[42] M. S. Arulampalam, S. Maskell, N. Gordon, and T. Clapp, "A tutorial on particle filters for online nonlinear/non-Gaussian Bayesian tracking," *IEEE Transactions on Signal Processing*, vol. 50, no. 2, pp. 174–188, Feb. 2002, doi: 10.1109/78.978374.

[43] M. Kaess, A. Ranganathan, and F. Dellaert, "iSAM: Fast incremental smoothing and mapping with efficient data association," *Proceedings - IEEE International Conference on Robotics and Automation*, pp. 1670–1677, 2007, doi: 10.1109/ROBOT.2007.363563.

[44] J. Ruppelt and G. F. Trommer, "Stereo-camera visual odometry for outdoor areas and in dark indoor environments," *IEEE Aerospace and Electronic Systems Magazine*, vol. 31, no. 11, pp. 4–12, Nov. 2016, doi: 10.1109/MAES.2016.150255.

[45] S. Rusinkiewicz and M. Levoy, "Efficient variants of the ICP algorithm," *Proceedings of International Conference on 3-D Digital Imaging and Modeling, 3DIM*, pp. 145–152, 2001, doi: 10.1109/IM.2001.924423.

[46] "IWR1443 Single-Chip 76-to 81-GHz mmWave Sensor 1 Device Overview," 2017, Accessed: Jan. 23, 2022. [Online]. Available: www.ti.com

[47] D. DAVID, P. GIANNI, G. FRANCESCO, and R. ELIA, "MILLIMETER WAVE RADAR FOR SLAM APPLICATIONS," 2020.

[48] F. Belloni, V. Ranki, A. Kainulainen, and A. Richter, "Angle-based indoor positioning system for open indoor environments," *Proceedings - 6th Workshop on Positioning, Navigation and Communication, WPNC 2009*, pp. 261–265, 2009, doi: 10.1109/WPNC.2009.4907836.

[49] A. Yassin *et al.*, "Recent Advances in Indoor Localization: A Survey on Theoretical Approaches and Applications," *IEEE Communications Surveys and Tutorials*, vol. 19, no. 2, pp. 1327–1346, Apr. 2017, doi: 10.1109/COMST.2016.2632427.

[50] S. Monfared, T. H. Nguyen, L. Petrillo, P. de Doncker, and F. Horlin, "Experimental Demonstration of BLE Transmitter Positioning Based on AOA Estimation," *IEEE International Symposium on Personal, Indoor and Mobile Radio Communications, PIMRC*, vol. 2018-September, pp. 856–859, Dec. 2018, doi: 10.1109/PIMRC.2018.8580796.

[51] M. C. Vanderveen, C. B. Papadias, and A. Paulraj, "Joint angle and delay estimation (JADE) for multipath signals arriving at an antenna array," *IEEE Communications Letters*, vol. 1, no. 1, pp. 12–14, 1997, doi: 10.1109/4234.552142.

[52] R. F. Brena, J. P. García-Vázquez, C. E. Galván-Tejada, D. Muñoz-Rodriguez, C. Vargas-Rosales, and J. Fangmeyer, "Evolution of Indoor Positioning Technologies: A Survey," *Journal of Sensors*, vol. 2017, 2017, doi: 10.1155/2017/2630413.

[53] F. Zafari, A. Gkelias, and K. K. Leung, "A Survey of Indoor Localization Systems and Technologies," *IEEE Communications Surveys and Tutorials*, vol. 21, no. 3, pp. 2568–2599, 2019, doi:

10.1109/COMST.2019.2911558.

[54] T. Bagosi and Z. Baruch, "Indoor localization by WiFi," *Proceedings - 2011 IEEE 7th International Conference on Intelligent Computer Communication and Processing, ICCP 2011*, pp. 449–452, 2011, doi: 10.1109/ICCP.2011.6047914.

[55] S. Boonsriwai and A. Apavatjrut, "Indoor WIFI localization on mobile devices," *2013 10th International Conference on Electrical Engineering/Electronics, Computer, Telecommunications and Information Technology, ECTI-CON 2013*, 2013, doi: 10.1109/ECTICON.2013.6559592.

[56] G. Deak, K. Curran, and J. Condell, "A survey of active and passive indoor localisation systems," *Computer Communications*, vol. 35, no. 16, pp. 1939–1954, Sep. 2012, doi: 10.1016/J.COMCOM.2012.06.004.

[57] S. Garcia-Villalonga and A. Perez-Navarro, "Influence of human absorption of Wi-Fi signal in indoor positioning with Wi-Fi fingerprinting," *2015 International Conference on Indoor Positioning and Indoor Navigation, IPIN 2015*, Dec. 2015, doi: 10.1109/IPIN.2015.7346778.

[58] I. Ashraf, S. Hur, and Y. Park, "Indoor Positioning on Disparate Commercial Smartphones Using Wi-Fi Access Points Coverage Area," *Sensors 2019, Vol. 19, Page 4351*, vol. 19, no. 19, p. 4351, Oct. 2019, doi: 10.3390/S19194351.

[59] P. C. Deepesh, V. N. Rao, R. Rath, N. Kanakalata, and A. Tiwary, "Experiences with using ibeacons for indoor positioning," *ACM International Conference Proceeding Series*, vol. 18-20-February-2016, pp. 184–189, Feb. 2016, doi: 10.1145/2856636.2856654.

[60] A. Dasgupta, R. Nagaraj, K. Nagamani, A. Dasgupta, R. Nagaraj, and K. Nagamani, "An Internet of Things Platform with Google Eddystone Beacons," *Journal of Software Engineering and Applications*, vol. 9, no. 6, pp. 291–295, Jun. 2016, doi: 10.4236/JSEA.2016.96020.

[61] A. Hameed and H. A. Ahmed, "Survey on indoor positioning applications based on different technologies," Jan. 2019. doi: 10.1109/MACS.2018.8628462.

[62] Z. Wei, Y. Zhao, X. Liu, and Z. Feng, "DoA-LF: A Location Fingerprint Positioning Algorithm with Millimeter-Wave," *IEEE Access*, vol. 5, pp. 22678–22688, Sep. 2017, doi: 10.1109/ACCESS.2017.2753781.

[63] D. Gualda, J. Ureña, J. Jesús García, A. Jiménez, M. Carmen Pérez, and F. Ciudad, "Coverage Analysis of an Ultrasonic Local Positioning System according to the Angle of Inclination of the Beacons Structure."

[64] A. Yassin, Y. Nasser, M. Awad, and A. Al-Dubai, "Simultaneous context inference and mapping using mm-Wave for indoor scenarios," Jul. 2017. doi: 10.1109/ICC.2017.7996976.

[65] F. Guidi, A. Guerra, and D. Dardari, "Millimeter-wave massive arrays for indoor SLAM," *2014 IEEE International Conference on Communications Workshops, ICC 2014*, pp. 114–120, 2014, doi: 10.1109/ICCW.2014.6881182.

[66] J. Palacios, G. Bielsa, P. Casari, and J. Widmer, "Single- and multiple-access point indoor localization for millimeter-wave networks," *IEEE Transactions on Wireless Communications*, vol. 18, no. 3, pp. 1927–1942, Mar. 2019, doi: 10.1109/TWC.2019.2899313.

[67] C. T. Li, J. C. P. Cheng, and K. Chen, "Top 10 technologies for indoor positioning on construction sites," *Automation in Construction*, vol. 118. Elsevier B.V., p. 103309, Oct. 01, 2020. doi: 10.1016/j.autcon.2020.103309.

[68] Z. Kong and Q. Lu, "A brief review of simultaneous localization and mapping," in *Proceedings IECON 2017 - 43rd Annual Conference of the IEEE Industrial Electronics Society*, Dec. 2017, vol. 2017-January, pp. 5517–5522. doi: 10.1109/IECON.2017.8216955.

[69] W. Lin, J. Hu, H. Xu, C. Ye, X. Ye, and Z. Li, "Graph-based SLAM in indoor environment using corner feature from laser sensor," in *Proceedings - 2017 32nd Youth Academic Annual Conference of Chinese Association of Automation, YAC 2017*, Jun. 2017, pp. 1211–1216. doi: 10.1109/YAC.2017.7967597.

[70] F. Zhang, S. Li, S. Yuan, E. Sun, and L. Zhao, "Algorithms analysis of mobile robot SLAM based on Kalman and particle filter," in *Proceedings of 2017 9th International Conference On Modelling, Identification and Control, ICMIC 2017*, Mar. 2018, vol. 2018-March, pp. 1050–1055. doi: 10.1109/ICMIC.2017.8321612.

[71] F. Hidalgo and T. Braunl, "Review of underwater SLAM techniques," in *ICARA 2015 - Proceedings of the 2015 6th International Conference on Automation, Robotics and Applications*, Apr. 2015, pp. 306–311. doi: 10.1109/ICARA.2015.7081165.

[72] B. Xi, R. Guo, F. Sun, and Y. Huang, "Simulation research for active simultaneous localization and mapping based on extended Kalman filter," in *Proceedings of the IEEE International Conference on Automation and Logistics, ICAL 2008*, 2008, pp. 2443–2448. doi: 10.1109/ICAL.2008.4636578.

[73] C. Stachniss, J. J. Leonard, and S. Thrun, "Simultaneous localization and mapping," in *Springer Handbook of Robotics*, Springer International Publishing, 2016, pp. 1153–1175. doi: 10.1007/978-3-319-32552-1_46.

[74] I. M. Rekleitis, "A particle filter tutorial for mobile robot localization," *International Conference on Robotics and*, vol. 3, no. TR-CIM-04-02, pp. 1–36, 2003, [Online]. Available: http://www4.cs.umanitoba.ca/~jacky/Teaching/Courses/74.795-LocalVision/ReadingList/rekleitis-particletutorial.pdf

[75] N. M. Yatim and N. Buniyamin, "Particle filter in simultaneous localization and mapping (Slam) using differential drive mobile robot," *Jurnal Teknologi*, vol. 77, no. 20, pp. 91–97, Sep. 2015, doi: 10.11113/jt.v77.6557.

[76] M. Chen, C. Bian, and Y. Jian Wu, "Research on Rao-Blackwillised Particle Filter SLAM algorithm based on QPSO," in *Chinese Control Conference, CCC*, Oct. 2018, vol. 2018-July, pp. 5179–5185. doi: 10.23919/ChiCC.2018.8483359.

[77] G. Grisetti, R. Kummerle, C. Stachniss, and W. Burgard, "A tutorial on graph-based SLAM," *IEEE Intelligent Transportation Systems Magazine*, vol. 2, no. 4, pp. 31–43, Dec. 2010, doi: 10.1109/MITS.2010.939925.

[78] E. Mendes, P. Koch, and S. Lacroix, "ICP-based pose-graph SLAM," in *SSRR 2016 - International Symposium on Safety, Security and Rescue Robotics*, Dec. 2016, pp. 195–200. doi: 10.1109/SSRR.2016.7784298.

[79] Y. Jia, X. Yan, and Y. Xu, "A Survey of simultaneous localization and mapping for robot," in *Proceedings of 2019 IEEE 4th Advanced Information Technology, Electronic and Automation Control Conference, IAEAC 2019*, Dec. 2019, pp. 857–861. doi: 10.1109/IAEAC47372.2019.8997820.

[80] M. Kaess, H. Johannsson, R. Roberts, V. Ila, J. J. Leonard, and F. Dellaert, "ISAM2: Incremental smoothing and mapping using the Bayes tree," *International Journal of Robotics Research*, vol. 31, no. 2, pp. 216–235, Feb. 2012, doi: 10.1177/0278364911430419.

[81] A. Aldroubi, K. Hamm, A. B. Koku, and A. Sekmen, "CUR Decompositions, Similarity Matrices, and Subspace Clustering," *Frontiers in Applied Mathematics and Statistics*, vol. 4, Jan. 2019, doi: 10.3389/fams.2018.00065.

[82] S. Konatowski, P. Kaniewski, and J. Matuszewski, "Comparison of Estimation Accuracy of EKF, UKF and PF Filters," *Annual of Navigation*, vol. 23, no. 1, pp. 69–87, 2017, doi: 10.1515/aon-2016-0005.

[83] Z. Kurt-Yavuz and S. Yavuz, "A comparison of EKF, UKF, FastSLAM2.0, and UKF-based FastSLAM algorithms," in *INES 2012 - IEEE 16th International Conference on Intelligent Engineering Systems, Proceedings*, 2012, pp. 37–43. doi: 10.1109/INES.2012.6249866.

[84] D. Wilbers, C. Merfels, and C. Stachniss, "A Comparison of Particle Filter and Graph-Based Optimization for Localization with Landmarks in Automated Vehicles," in *Proceedings - 3rd IEEE International Conference on Robotic Computing, IRC 2019*, Mar. 2019, pp. 220–225. doi: 10.1109/IRC.2019.00040.

[85] M. Holder, S. Hellwig, and H. Winner, "Real-time pose graph SLAM based on radar," in *IEEE Intelligent Vehicles Symposium, Proceedings*, Jun. 2019, vol. 2019-June, pp. 1145–1151. doi: 10.1109/IVS.2019.8813841.

[86] S. H. Cen, "Ego-Motion Estimation and Localization with Millimeter-Wave Scanning Radar."

[87] Elia F, "MILLIMETER WAVE RADAR FOR SLAM APPLICATIONS".

[88] Texas Instruments, "IWR1443-Doxygen".

[89] C. He, C. Tang, and C. Yu, "A Federated Derivative Cubature Kalman Filter for IMU-UWB Indoor Positioning," *Sensors 2020, Vol. 20, Page 3514*, vol. 20, no. 12, p. 3514, Jun. 2020, doi: 10.3390/S20123514.

[90] A. Poulose and D. S. Han, "Hybrid Indoor Localization Using IMU Sensors and Smartphone Camera," *Sensors 2019, Vol. 19, Page 5084*, vol. 19, no. 23, p. 5084, Nov. 2019, doi: 10.3390/S19235084.

[91] M. A. al Mamun and M. Rasit Yuce, "Map-Aided Fusion of IMU PDR and RSSI Fingerprinting for Improved Indoor Positioning," pp. 1–4, Dec. 2021, doi: 10.1109/SENSORS47087.2021.9639778.

[92] Paul J. Besl and Neil D. McKay, "Method for registration of 3-D shapes." https://www-spiedigitallibrary-org.ezproxy.auckland.ac.nz/conference-proceedings-of-spie/1611/1/Method-for-registration-of-3-D-shapes/10.1117/12.57955.full?SSO=1 (accessed Feb. 19, 2022).

[93] H. M. Kjer and J. Wilm, "Evaluation of surface registration algorithms for PET motion correction," 2010, Accessed: Mar. 27, 2022. [Online]. Available: www.imm.dtu.dk

[94] G. Godin, M. Rioux, and R. Baribeau, "Three-dimensional registration using range and intensity

information," *https://doi.org/10.1117/12.189139*, vol. 2350, pp. 279–290, Oct. 1994, doi: 10.1117/12.189139.

[95] TEXAS INSTRUMENTS, "mmw Demo Data Structure v0.1."